PERFORMANCE OF MONOCOQUE AND SEMI-MONOCOQUE COMPOSITE POLES FOR TRANSMISSION LINES

Plínio Ricardo dos Santos

UNIVERSIDADE FEDERAL DE MINAS GERAIS
ESCOLA DE ENGENHARIA
PROGRAMA DE PÓS-GRADUAÇÃO EM ENGENHARIA DE ESTRUTURAS

"PERFORMANCE OF MONOCOQUE AND SEMI-MONOCOQUE COMPOSITE POLES FOR TRANSMISSION LINES"

Plínio Ricardo dos Santos

Dissertação apresentada ao Programa de Pós-Graduação em Engenharia de Estruturas da Escola de Engenharia da Universidade Federal de Minas Gerais, como parte dos requisitos necessários à obtenção do título de "Mestre em Engenharia de Estruturas".

Comissão Examinadora:

_____
Prof. Dr. Carlos Alberto Cimini Jr.
DEES - UFMG (Orientador)

_____
Prof. Dr. Estevam Barbosa de Las Casas
DEES - UFMG

_____
Prof. Dr. Leandro José da Silva
UFSJ

Belo Horizonte, 27 de junho de 2018

Santos, Plínio Ricardo dos.
S237p Performance of monocoque and semi-monocoque composite poles for transmission lines [manuscrito] / Plínio Ricardo dos Santos. – 2018.
xii, 51 f., enc.: il.

Orientador: Carlos Alberto Cimini Júnior.

Dissertação (mestrado) Universidade Federal de Minas Gerais, Escola de Engenharia.

Bibliografia: f. 49-51.

1. Engenharia de estruturas - Teses. 2. Postes (Engenharia) - Teses. 3. Materiais compostos - Teses. I. Cimini Júnior, Carlos Alberto. II. Universidade Federal de Minas Gerais. Escola de Engenharia. III. Título.

DU:624(043)

ACKNOWLEDGEMENTS

Firstly, I would like give thanks to God for protect my way and for all the achievements.

I would like to express my sincere gratitude to my advisor Professor Dr. Carlos Alberto Cimini Jr. for the all support in this hard journey. I will be forever grateful. There could be no other comparable support.

I would also like to thank my parents, friends and all my family for their support and incentive.

Thanks to all my friends from MECBIO, especially Professor Dr. Estevam Barbosa de Las Casas for technical support.

Thanks to all my friends from PROPEEs who have made this journey become happier.

I would also like to thank all my friends at UFSJ who have been part of my journey.

RESUMO

Os postes têm importante finalidade na distribuição de energia elétrica. Outros setores como de telefonia e internet também utilizam esse suporte para levar seus serviços às residências. Atualmente, os postes são constituídos de madeira, concreto armado e aço. No entanto, estes materiais estão sujeitos a problemas, como rápida degradação da madeira, grande peso e difícil instalação para postes de concreto armado, além da corrosão no aço. Algumas alternativas são adotadas para minimizar esses problemas, como tratamento da madeira, otimização das estruturas de concreto e proteção da superfície dos aços. Outra alternativa é buscar diferentes tipos de materiais que supram os requisitos necessários para utilização desses postes. Os materiais compostos, como os polímeros reforçados por fibras de vidro (PRFV), têm grandes vantagens por serem resistentes, leves e isolantes. Estruturas do tipo monocoque e semi-monocoque (utilizadas em fuselagens de aeronaves) permitem a redução na massa final, o que combinado com o uso de materiais compostos gera estruturas ainda mais leves. Neste trabalho, quatro configurações de estruturas monocoque e semi-monocoque (com uso de reforçadores longitudinais e anéis transversais) em diferentes combinações são analisadas. Para isso, um estudo paramétrico identifica configurações favoráveis que são estudadas posteriormente. Utiliza-se o método das diferenças finitas para o cálculo das flechas máximas, a fim de se avaliar a rigidez adequada. A estabilidade estrutural e a resistência são analisadas utilizando o *software* comercial de elementos finitos Abaqus™. Observa-se que para ângulos das fibras próximos aos ângulos dos eixos longitudinais dos postes, as massas resultantes para os postes semi-monocoque diferem pouco dos postes monocoque. No entanto para ângulos maiores, existe uma diferença significativa nas massas, o que torna mais leves os postes semi-monocoque. Quando adicionados os anéis ou quando estes são combinados com os reforçadores, houve um aumento considerável na resistência do poste.

Palavras-chave: Postes; Materiais Compostos; PRFV; Monocoque; Semi-monocoque**.**

ABSTRACT

Poles play an important role in distribution of electrical energy. Other sectors such as telephone and internet also use their support to bring services to homes. Currently, poles are made of wood, reinforced concrete and steel. However, these materials are subject to problems such as rapid wood degradation, high weight and difficult installation for reinforced concrete poles and corrosion in steels. Some alternatives are adopted to minimize these problems, such as wood treatment, optimization of concrete structures and protection of steel surfaces. Another alternative is to look for different types of materials to supply all pole requirements. Composite materials, such as glass fiber-reinforced polymer (GFRP), have great advantages because they are resistant, light and insulating. Monocoque and semi-monocoque (commonly used in aircraft fuselages) structures allow reduction the final mass, which combined with the use of composite materials generates even lighter structures. In this work, four configurations of monocoque and semi-monocoque (using longitudinal stringers and transverse ring) structures in different combinations are analyzed. A parametric study identifies favorable configurations, which are later studied. The finite difference method is used for the calculation of the maximum deflections, to evaluate the adequate stiffness. The structural stability and the strength are analyzed using the commercial finite element software Abaqus™. It is observed that, for fiber angles near the longitudinal pole axes, the resulting masses for the semi-monocoque poles differ little from the monocoque poles. However, for larger angles, there is a significant difference in the masses, which makes the semi-monocoque poles lighter. When rings are added or when these are combined with the stringers, there is a considerable increase on the pole ultimate strength.

Keywords: Poles; Composite Materials; GFRP; Monocoque; Semi-monocoque.

TABLE OF CONTENTS

LIST OF FIGURES

LIST OF TABLES

LIST OF NOMENCLATURE

α - Coefficient of shear stress contribution to fiber tensile criterion of Hashin Initiation Criterion;

σ_{11} – Longitudinal normal stress;

σ_{22} – Transverse normal stress;

σ_{12} – In-plane shear stress;

$\hat{\sigma}_{11}$- Longitudinal normal effective stress;

$\hat{\sigma}_{22}$ - Transverse normal effective stress;

$\hat{\sigma}_{6}$ - In-plane shear effective stress;

$E_{||}$- undamaged Young's modulus in the fiber direction;

$E_{\perp}$- undamaged Young's modulus in the direction perpendicular to the fibers;

K^{MN} - Tangent stiffness matrix;

Q^{N}- Incremental load;

d_f - Damage variables for fiber;

d_m - Damage variables for matrix;

d_s- Damage variables for shear;

$\boldsymbol{K}_0^{NM}$ - Stiffness matrix corresponding to the base state, which includes the effects of the preloads;

$\boldsymbol{K}_{\Delta}^{NM}$ - Differential initial stress and load stiffness matrix due to the incremental loading pattern;

λ_j - Critical buckling (eigenvalues);

v_{12} – Poisson's ratio associated with loading in the 1-direction and strain in the 2-direction;

v_{21}- Poisson's ratio associated with loading in the 2-direction and strain in the 1-direction;

F_{1t} – Longitudinal tensile strength;

F_{1c} – Longitudinal compressive strength;

F_{2t} – Transverse tensile strength;

F_{2c} – Transverse compressive strength;

v_j^M - Buckling mode shapes (eigenvectors);

[T] - Transformation matrix;

123 – Local coordinate system;

E - Modulus of elasticity;

E_1 – Longitudinal modulus (in local 1-direction);

E_2 – Transverse modulus (in local 2-direction);

F_{12} or F_6 is shear strength allowable in 12 plane;

F_{23} denotes the transverse shear strength;

G- undamaged shear modulus;

G_{12} – Shear modulus;

h - Distance between two neighboring nodes;

HSNFCCRT - Maximum value of the fiber compressive initiation criterion experienced;

HSNFTCRT - Maximum value of the fiber tensile initiation criterion experienced;

HSNMCCRT - Maximum value of the matrix compressive initiation criterion experienced;

HSNMTCRT - Maximum value of the matrix tensile initiation criterion experienced;

I - Inertia of the cross section;

j - *j*th buckling mode;

M - Bending moment;

M and *N* - Degrees of freedom;

U1 – Displacement in x axes;

U2 – Displacement in y axes;

U3 – Displacement in z axes;

UR1 – Rotation about x axes;

UR2 – Rotation about y axes;

UR3 – Rotation about z axes;

w - Beam transverse displacement;

xyz – Global coordinate system;

ρ - material density;

$\boldsymbol{\epsilon}$ - strain tensor.

LIST OF ACRONYMS

GFRP – Glass Fiber reinforced Polymer

PRFV– Polímeros Reforçados por Fibras de Vidro

FEM – Finite Element Method

FDM – Finite Difference Method

CFRP – Carbon Fiber Reinforced Polymer

FPF – First ply failure

ULF – Ultimate laminate failure

1

INTRODUCTION

Poles are structures positioned vertically to support, mainly, the transmission and distribution lines of electrical energy. Other kinds of distribution are also supported by poles, such as telephone and internet lines, making them important in these sectors. Furthermore, poles also have function in lighting, especially in public lighting.

Poles are traditionally manufactured in wood, steel or steel reinforced concrete. However, there are some disadvantages on the use of these materials. The use of wood, for example, generates limitation in final height, besides being prone to attack by fungi and bacteria. Poles made by concrete are heavier, leading to transport and installation problems. Steel presents greater weight and electric conductivity and, in addition, corrosion problems (Metiche and Masmoudi, 2012). To overcome some of these problems, manufacturers and designers seek other alternatives, such as the use of galvanization and paints to avoid corrosion and degradation, and optimization to reduce weight. Another alternative is the search for new applications of materials that meet conditions imposed by the electrical system, such as the composite materials.

The applications of composite materials, such as Carbon Fiber Reinforced Polymer (CFRP) and Glass Fiber Reinforced Polymer (GFRP), have been frequent, driven by the requirement for lightweight and more flexible structures in the aerospace industry. Structures of thin shells, where the outer surface is usually supported by longitudinal stiffening elements (stringers) and transverse rings, are called semi-monocoque (Megson, 1999). This allows better resistance to the compression loads, bending and torsion, postponing buckling and material failure. Structures that depend only on shells to resist stresses are called monocoque (Megson, 1999). Semi-monocoque structures are common in aircraft fuselages (Figure 1) due to required weight restrictions.

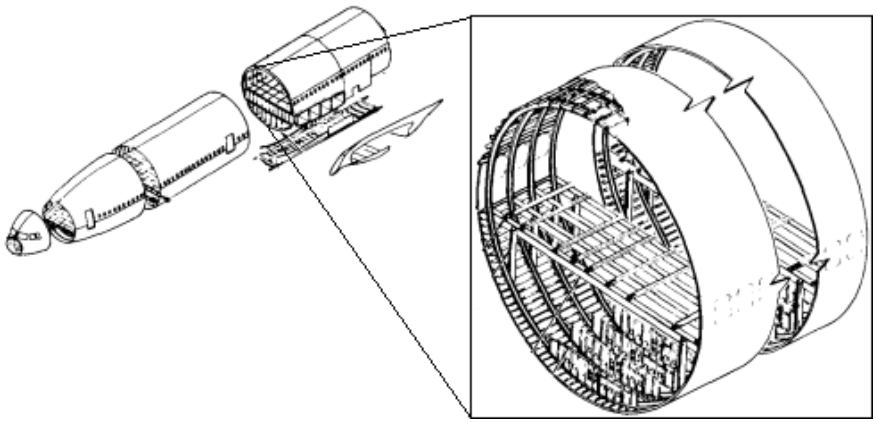

Figure 1: Semi-monocoque fuselage (adapted from Niu, 1988)

Recently the use of composite materials has been the solution not only in the aerospace industry, where these materials stand out, but also in the automotive and in civil construction industries. In Brazil, Petrofisa do Brasil Ltda. produces GFRP poles in the monocoque configuration. According to their available data, the poles manufactured have higher costs when compared with concrete poles. However, when analyzed in a global context, considering transportation, installation and maintenance costs, the final cost is lower. In addition, it is possible to repair the pole in case of impact by vehicles, not requiring the complete exchange of the product, a fact that does not occur in concrete poles (Petrofisa do Brasil, 2008). Another interesting aspect of the GFRP poles is safety for the drivers and less damage to the vehicle in case of an impact, because the GFRP absorbs more energy, as seen in Figure 2.

Figure 2: Crash test to evaluate the pole behavior (Globo Play, 2017)

2

OBJECTIVES

The purpose of this work is to analyze the performance of different configurations of Glass Fiber Reinforced Polymer (GFRP) monocoque and semi-monocoque composite poles for application in electric power distribution networks. For semi-monocoque configurations, the poles are analyzed with longitudinal stringers and rings, investigating the quantity of each. Analysis encompass the ability to resist stresses, which can cause both buckling and material failure. Very flexible poles can cause problems such as maintenance difficulties in the electrical network and cable tensioning. Therefore, in this work, the pole stiffness is also an important parameter to be considered.

The fibers directions have a significant effect on the pole performance, since the GFRP has greater stiffness and resistance in the fibers directions. Consequently, it is expected that the skin thickness needed to resist the stresses will be smaller when the angles between the fibers and the longitudinal axis of the pole are smaller. Thus, in this work, the pole behavior is evaluated by varying the fiber angles, in order to relate them to the shell thickness, and, consequently, to the resulting pole mass.

Currently in the literature there are many works on monocoque poles and a few on semi-monocoque poles with longitudinal stringers, as it will be shown in the next section. In this work, the addition of rings is included for a new type of configuration. Thus, a comparison is made between all possible configurations presented in Table 1, which will demonstrate the main advantages and disadvantages of each configuration.

Table 1: Proposed pole conditions

Condition	Stringers	Rings
A	Without	Without
B	With	Without
C	Without	With
D	With	With

3

LITERATURE REVIEW

3.1. Composite poles

Ibrahim (2000) in his thesis, tapered GFRP poles was evaluated in a monocoque configuration for transmission lines. Twelve scaled poles with 2.5 m and 12 full-scale poles with 6.1 m under lateral loads were tested and numerically analyzed. The load-deflection behavior, the natural frequency and period of fundamental frequency vibration mode were computed. A parametric study was conducted to analyze the effect of wall thickness, fiber orientation and diameter. According to the results, the poles can be designed to support the same load capacity as wood, concrete or steel poles with smaller masses. The scaled specimens (2.5 m long) with radius-to-thickness ratio (R/t) equal to 57 failed by local buckling on the compression side and scaled specimens with R/t ratio equal to 40 or 23 failed by material failure. For the full scale, R/t varied from 42 to 75; ten failed by local buckling and two by material failure. The same authors published results in Polyzois et al. (1999) and Ibrahim et al. (2001).

Metiche and Masmoudi (2012) designed and tested small poles for lighting (Figure 3), with heights varying from 5 to 12 meters using simple structures of glass fibers in the polymer matrix without internal stringers (monocoque structure). The tests were conducted on a bench in order to apply bending loads and axial loads. The axial loads acting separately had no significant influence on local buckling. However, combined loads were considered: bending, compression and shear. For relations (E I) / (L ρ) at the base greater than 23.5 kN·m² / g (where E is the longitudinal modulus of elasticity, I is the moment of inertia, L is the height and ρ is the linear

density), the material failures occur directly at the bottom. Another possibility of failure was local buckling, which occurred near to the openings.

Figure 3: Pole studied by Metiche e Masmoudi (2012)

Fam et al. (2010) investigated, using the finite element method, the response of GFRP tubes for application on poles. The parametric study considered axial and lateral loads and different fiber angles (Figure 4). The axial strength increases when fiber angles close the longitudinal axis. Similar effect occurred for flexural strength, but this became more evident for smaller diameter/thickness ratios. Material failures were observed and the global buckling was accentuated with the increase L / D ratio and the local buckling was accentuated increasing D/t, as expected. To validate the method, the authors compared numerical results with experimental results presented by Ibrahim (2000) and Fam (2000), mentioned posteriorly.

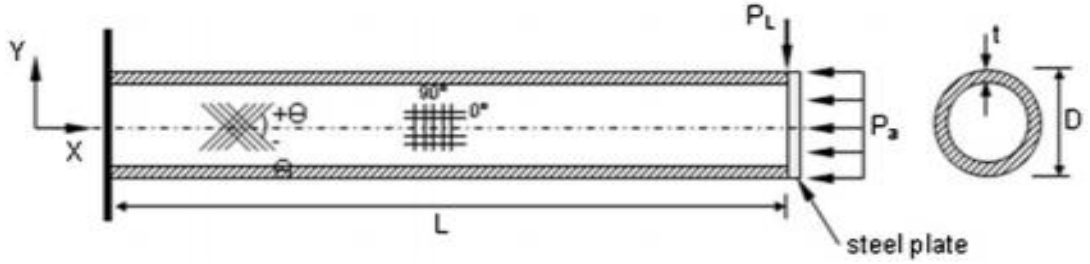

Figure 4: Pole studied by Fam et al. (2010)

Birchal (2001) studied poles of constant cross sections composed of two concentric cylinders (outer skin and inner skin), reinforced by longitudinal stringers between the cylinders, as represented in Figure 5. The results showed lighter poles when compared with monocoque metallic poles, monocoque composite poles and metal transmission towers. Cimini et al. (2005), constructed and tested, through a four-point test, the pole configurations studied by Birchal (2001) and Birchal et al. (2001) made from glass fibers / polyester. The results showed good agreement with the design for strength and stiffness.

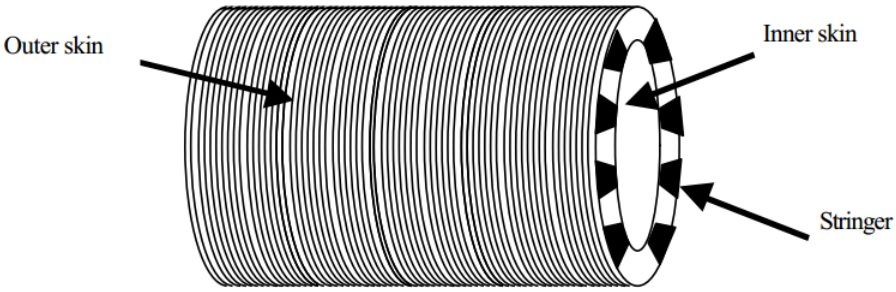

Figure 5: Pole design concept studied by Birchal (2001) and Birchal et al. (2001)

Cimini and Las Casas (2013) have patented a constructive arrangement for fiber reinforced polymer composite poles using the semi-monocoque configuration. The configuration is shown in Figure 6 and consists of a skin made by filament winding, and internal stringers bonded to the skin, manufactured by pultrusion. The configuration differs from the model shown in Figure 5 why it does not have the inner cylinder, simplifying the constructive process. The stringers are positioned in a mandrel with grooves; then, the process of filament winding is done, bonding stringer and skin.

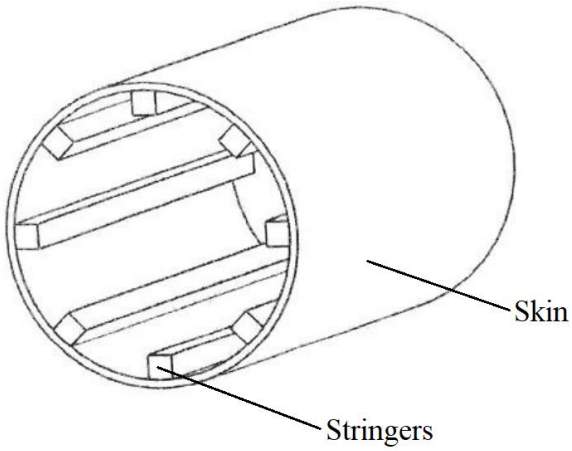

Figure 6: Pole design concept patented by Cimini and Las Casas (adapted from Cimini and Las Casas, 2013)

Alípio (2014), studied three different types of poles. The first consisted of a semi-monocoque pole made of E-Glass fibers and polyester matrix with the same configuration shown in Figure 6. The second was monocoque, made of the same material. And the third was a massive pole of reinforced concrete. As the base and top diameters considered were different, the author used the finite difference method to solve Bernoulli-Euler's differential equations and thus calculate the deflection, which were compared to the results of simulation using Abaqus™ commercial software. The results showed an intermediate maximum deflection of the semi-monocoque

pole, with a lower weight and a higher safety factor. The third pole, besides presenting a mass of about seven times greater than the first, had the lowest safety factor. The results are given in Table 2 (the deflections in parentheses are experienced as a percentage of the pole length).

Table 2: Results obtained by Alípio (2014)

	First model	Second model	Third model
Lower safety factor	15.22	2.23	2.10
Maximum deflection	515.00 mm (4.29 %)	1159.60 mm (9.66 %)	148.30 mm (1.23 %)
Mass	231.00 kg	235.60 kg	1656.40 kg

3.2. Pole deflection

One of the criteria for designing poles for transmission and distribution of electricity is the stiffness. According to CEMIG (2010), the maximum deflection allowed at the top is five per cent of the nominal length. Alípio (2014) implemented a program based on the Finite Difference Method to solve the pole deflection. In this case, the Bernoulli-Euler's equations (Hibbeler, 2010), given by (1), is solved.

$$M = EI \frac{\partial^2 w}{\partial x^2} \tag{1}$$

where M is the bending moment, E is the modulus of elasticity, I is the inertia of the cross section, w is the beam transverse displacement and the x-axis is oriented in the longitudinal direction. For constant sections and small displacements, we can easily calculate the displacement due to a transverse load solving (1). However, in the case of the tapered poles, it is necessary to use a numerical method.

3.2.1. Finite Difference Method

When the geometry of the problem does not favor the analytical solution, numerical methods, such as the Finite Element Method (FEM), are used. Another existing method is the Finite Differences Method (FDM), which is a numerical way of approaching the solution of differential equations using the Taylor series. Soares (2010) evaluated the convergence of this method applied to the Bernoulli-Euler beams theory, obtaining results with great precision. According to Cunha (2000), to apply the method, we must first discretize the region where the solution is sought. This is a common procedure when numerical methods are used to solve

differential equations. We define the mesh as a set of points, which are called nodes of the mesh. Then, the derivatives that appear in the differential equation are discretized. The derivatives will be approximated by differences between discretized solution values.

Using the Taylor series, we evaluate a function *y (x)* in the neighborhood of a point *x*, that is, at the point *x* + *h*, given by (2):

$$y(x+h) = \sum_{i=0}^{n} \frac{h^i}{i!} y^{(i)}(x) \tag{2}$$

There are three strategies to discretize derivatives using the Taylor series expansion. The first is called the forward formula, and consists of adopting *n* = 1 in (2), thus:

$$y(x+h) = \frac{h^0}{0!} y^{(0)}(x) + \frac{h^1}{1!} y^{(1)}(x) \tag{3}$$

Isolating the first derivative:

$$y'(x) = \frac{y(x+h) - y(x)}{h} \tag{4}$$

In this case *h* is the distance between two neighboring nodes. Taking -*h* in (2) and adopting *n* =1, through the same procedure, we have the backward formula:

$$y'(x) = \frac{y(x) - y(x-h)}{h} \tag{5}$$

The central formula consists of evaluating Taylor's expansion at both points *x* + *h* and *x*-*h*, using n = 2:

$$y'(x) = \frac{y(x+h) - y(x-h)}{2h} \tag{6}$$

One way to approach a solution from (2) is to make *n* = 3 and evaluate the Taylor expansion at points *x* + *h* and *x* - *h*, which gives two equations, which, when combined, result in:

$$y''(x) = \frac{y(x+h) - 2y(x) + y(x-h)}{h^2} \tag{7}$$

Considering now the beam of Figure 7, with *n* nodes, it follows that, by isolating the second derivative of the Bernoulli-Euler equation:

$$w'' = \frac{M}{EI} \tag{8}$$

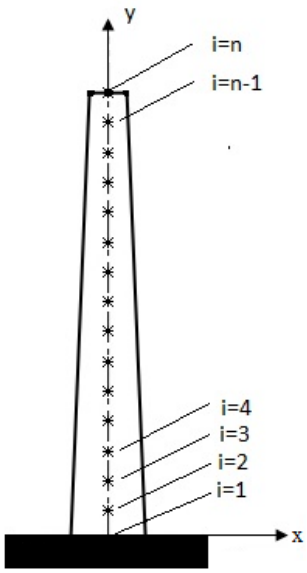

Figure 7: Discretized problem

Thus, for each node *i*:

$$\begin{cases} i = 1 \quad \rightarrow \quad w''_1 = \dfrac{M_1}{E_1 I_1} \\ i = 2 \quad \rightarrow \quad w''_2 = \dfrac{M_2}{E_2 I_2} \\ i = 3 \quad \rightarrow \quad w''_3 = \dfrac{M_3}{E_3 I_3} \\ \quad\quad\quad\quad . \\ \quad\quad\quad\quad . \\ \quad\quad\quad\quad . \\ i = n-2 \quad \rightarrow \quad w''_{n-2} = \dfrac{M_{n-2}}{E_{n-2} I_{n-2}} \\ i = n-1 \quad \rightarrow \quad w''_{n-2} = \dfrac{1}{E_{n-1} I_{n-1}} \\ i = n \quad \rightarrow \quad w''_{n-3} = \dfrac{M_n}{E_n I_n} \end{cases} \tag{9}$$

According to (7):

$$w'' = \frac{w(x+h) - 2w(x) + w(x-h)}{h^2} \tag{10}$$

or:

$$w'' = \frac{w_{i+1} - 2w_i + w_{i-1}}{h^2} \tag{11}$$

Replacing the (11) in the system of equation (9):

$$\begin{cases} i = 1 \quad \rightarrow \quad w_2 - 2w_1 + w_0 = \dfrac{h^2 M_1}{E_1 I_1} \\ i = 2 \quad \rightarrow \quad w_3 - 2w_2 + w_1 = \dfrac{h^2 M_2}{E_2 I_2} \\ i = 3 \quad \rightarrow \quad w_4 - 2w_3 + w_2 = \dfrac{h^2 M_3}{E_3 I_3} \\ \vdots \\ i = n-2 \quad \rightarrow \quad w_{n-1} - 2w_{n-2} + w_{n-3} = \dfrac{h^2 M_{n-2}}{E_{n-2} I_{n-2}} \\ i = n-1 \quad \rightarrow \quad w_n - 2w_{n-1} + w_{n-2} = \dfrac{h^2 M_{n-1}}{E_{n-1} I_{n-1}} \\ i = n \quad \rightarrow \quad w_{n+1} - 2w_n + w_{n-1} = \dfrac{h^2 M_n}{E_n I_n} \end{cases} \tag{12}$$

After this procedure, the boundary conditions are replaced. In this case w_0 e w_1 are zero, due the fixed base. In the free end, we have that the bending moment is also zero (Silva, 2008), resulting:

$$\frac{h^2 M_n}{E_n I_n} = 0 \tag{13}$$

Rewriting:

$$\begin{cases} i = 1 \quad \rightarrow \quad -2w_1 = \dfrac{h^2 M_1}{E_1 I_1} \\ i = 2 \quad \rightarrow \quad w_3 - 2w_2 = \dfrac{h^2 M_2}{E_2 I_2} \\ i = 3 \quad \rightarrow \quad w_4 - 2w_3 + w_2 = \dfrac{h^2 M_3}{E_3 I_3} \\ \vdots \\ i = n-2 \quad \rightarrow \quad w_{n-1} - 2w_{n-2} + w_{n-3} = \dfrac{h^2 M_{n-2}}{E_{n-2} I_{n-2}} \\ i = n-1 \quad \rightarrow \quad w_n - 2w_{n-1} + w_{n-2} = \dfrac{h^2 M_{n-1}}{E_{n-1} I_{n-1}} \\ i = n \quad \rightarrow \quad 0 = \dfrac{h^2 M_n}{E_n I_n} \end{cases} \tag{14}$$

We can rewrite the right side of the equations as:

$$C_i = \frac{h^2 M_i}{E_i I_i} \tag{15}$$

or in matrix form:

$$\begin{pmatrix} 0 & 0 & 0 & 0 & 0 & 0 & & & & & \\ 0 & -2 & 1 & 0 & 0 & 0 & & & & & \\ 0 & 1 & -2 & 1 & 0 & 0 & \cdots & & \cdots & & \\ 0 & 0 & 1 & -2 & 1 & 0 & & & & & \\ 0 & 0 & 0 & 1 & -2 & 1 & & & & & \\ & & \vdots & & & & \ddots & & \vdots & & \\ & & & & & & 1 & -2 & 1 & 0 & 0 \\ & & \cdots & & & & 0 & 1 & -2 & 1 & 0 \\ & & & & & & 0 & 0 & 1 & -2 & 1 \\ & & & & & & 0 & 0 & 0 & 0 & 0 \end{pmatrix} \begin{pmatrix} w_1 \\ w_2 \\ w_3 \\ w_4 \\ w_5 \\ \vdots \\ w_{n-3} \\ w_{n-2} \\ w_{n-1} \\ w_n \end{pmatrix} = \begin{pmatrix} C_1 \\ C_2 \\ C_3 \\ C_4 \\ C_5 \\ \vdots \\ C_{n-3} \\ C_{n-2} \\ C_{n-1} \\ C_n \end{pmatrix} \tag{16}$$

Isolating the vector of nodal displacement:

$$\begin{pmatrix} w_1 \\ w_2 \\ w_3 \\ w_4 \\ w_5 \\ \vdots \\ w_{n-3} \\ w_{n-2} \\ w_{n-1} \\ w_n \end{pmatrix} = \begin{pmatrix} 0 & 0 & 0 & 0 & 0 & 0 & & & & & \\ 0 & -2 & 1 & 0 & 0 & 0 & & & & & \\ 0 & 1 & -2 & 1 & 0 & 0 & \cdots & & \cdots & & \\ 0 & 0 & 1 & -2 & 1 & 0 & & & & & \\ 0 & 0 & 0 & 1 & -2 & 1 & & & & & \\ & & \vdots & & & & \ddots & & \vdots & & \\ & & & & & & 1 & -2 & 1 & 0 & 0 \\ & & \cdots & & & & 0 & 1 & -2 & 1 & 0 \\ & & & & & & 0 & 0 & 1 & -2 & 1 \\ & & & & & & 0 & 0 & 0 & 0 & 0 \end{pmatrix}^{-1} \begin{pmatrix} C_1 \\ C_2 \\ C_3 \\ C_4 \\ C_5 \\ \vdots \\ C_{n-3} \\ C_{n-2} \\ C_{n-1} \\ C_n \end{pmatrix} \tag{17}$$

Then, to find the nodal displacements, the beam is discretized and the coefficients C_i of (15) for each point are determined and replaced in (17).

3.3. Composite materials - Fiber reinforced polymer

According to Daniel e Ishai (2006), a structural composite is defined as a material system composed of two or more phases, designed to provide superior properties to the same materials acting independently (although it is better to say "different" rather than "superior" properties). In general, one of the phases is discontinuous and more resistant, called "reinforcement" and the less resistant phase is called "matrix". Sometimes, due to some chemical interactions or effects of other processes, an additional distinct phase exists between the matrix and the reinforcement, called the interface (Figure 8).

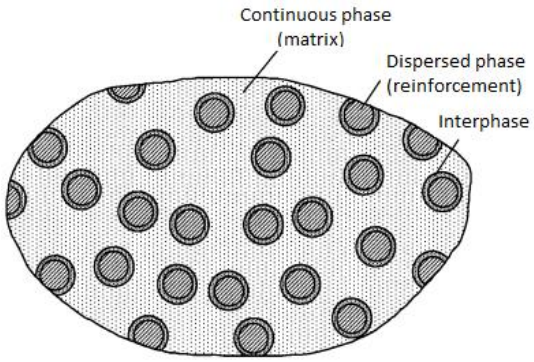

Figure 8: Phases of a composite material (adapted from Daniel and Ishai, 2006)

3.3.1. Mechanics of composite materials

A lamina or ply is a plane or curved layer of fibers in a matrix. The principal axes are designated 1, 2 and 3, where the axis 1 is parallel to the fibers, the axis 2 is transverse to the fibers and axis 3 is normal to the plane formed by axes 1 and 2, as shown in Figure 9a. The laminate is made up of two or more laminae staked together at various directions. For this case, the axes system adopt are x, y and z. The directions of the fibers are represented by the angle with respect to the x-axis, as exemplified in Figure 9b (Daniel and Ishai, 2006).

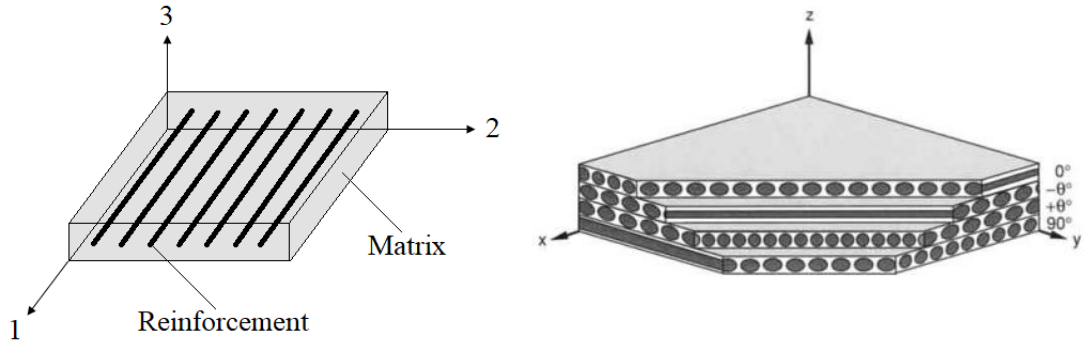

(a) (b)

Figure 9: Axes of a (a) lamina (elaborated by the author) and (b) laminate (Daniel e Ishai, 2006)

When the main reference axes of the material (1, 2 and 3) does not coincide with the axes related to the loading (x, y and z), as shown in Figure 9b, it is possible to relate both state of stress through the transformation matrix [T], according to (18), (19) and (20) for plane stress (see Figure 10).

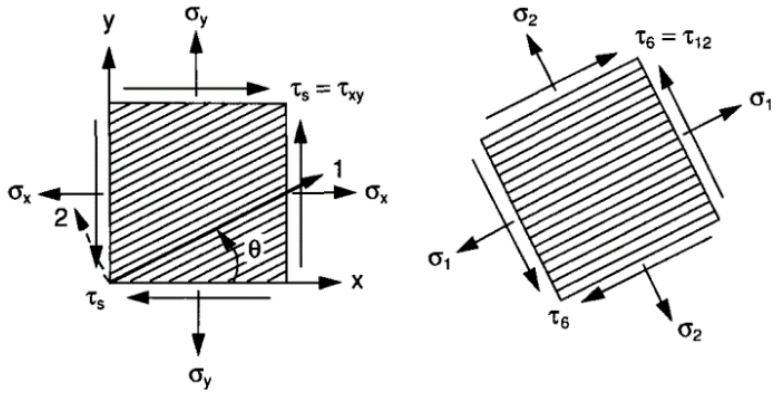

a) b)

Figure 10: Stress components referred to a) load and b) material axes (adapted from Daniel e Ishai, 2006)

$$\begin{bmatrix}\sigma_1\\ \sigma_2\\ \tau_6\end{bmatrix} = [T]\begin{bmatrix}\sigma_x\\ \sigma_y\\ \tau_{xy}\end{bmatrix} \tag{18}$$

where:

$$[T] = \begin{bmatrix} m^2 & n^2 & 2mn \\ n^2 & m^2 & -2mn \\ -mn & mn & m^2 - n^2 \end{bmatrix} \tag{19}$$

$$m = cos(\theta), n = sin(\theta) \quad (20)$$

and σ_1, σ_2, τ_6 are components of state of stress referred to material axes and σ_x, σ_y τ_6 referred to load axes.

3.3.2. Progressive failure

In most cases, the failure of fiber reinforced composite has a dominant mode. Hashin and Rotem (1973) and Hashin (1980), proposed failure criteria based in four different modes: fiber tension, fiber compression, matrix tension and matrix compression. Table 3 shows the load cases and failure equations proposed for each mode.

According to Matzenmiller et al. (1995), the elastic-brittle behavior of many composite materials is characterized by formation and evolution of microcracks and cavities, causing stiffness degradation. This case, damage plays an important role.

The progressive failure consists of formation and evolution of microcracks and cavities up to a limiting crack density. Following this first ply failure (FPL), the failure process continues, with a load redistribution, up to ultimate laminate failure (UPF) (Daniel and Ishai, 2006).

The software Abaqus™ offers tools to analyze the Progressive Damage and Failure in composite materials. The model is based on Hashin theory (Hashin and Rotem, 1973 and Hashin, 1980) to detect the failure (Damage Initiation). Hashin and Rotem equations are expressed in terms of effective stresses, according to (21).

Table 3: Failure criteria adopted (the figures were obtained from Doitrand et al., 2015)

Description	Equation	Load Case
Fiber tension, $\hat{\sigma}_{11} \geq 0$	$F_f^t = \left(\frac{\hat{\sigma}_{11}}{F_{1t}}\right)^2 + \alpha\left(\frac{\hat{\sigma}_6}{F_6}\right)^2$	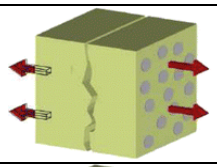
Fiber compression, $\hat{\sigma}_{11} < 0$	$F_f^c = \left(\frac{\hat{\sigma}_{11}}{F_{1c}}\right)^2$	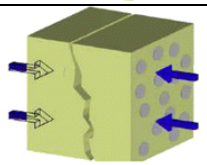
Matrix tension, $\hat{\sigma}_{22} \geq 0$	$F_m^t = \left(\frac{\hat{\sigma}_{22}}{F_{2t}}\right)^2 + \left(\frac{\hat{\sigma}_6}{F_6}\right)^2$	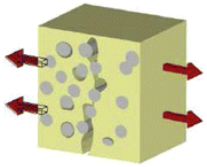
Matrix compression, $\hat{\sigma}_{22} < 0$	$F_m^c = \left(\frac{\hat{\sigma}_{22}}{2F_{23}}\right)^2 + \left[\left(\frac{F_{2c}}{2F_{23}}\right)^2 - 1\right]\frac{\hat{\sigma}_{22}}{F_{2c}} + \left(\frac{\hat{\sigma}_6}{F_6}\right)^2$	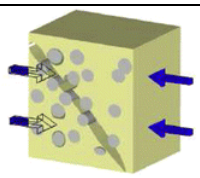

The laminate composite properties are defined as:

F_{1t} is tensile strength allowable parallel to filament;
F_{1c} is compression strength allowable parallel to filament;
F_{2t} is tensile strength allowable transverse to filament;
F_{2c} is compression strength allowable transverse to filament;
F_{12}or F_6 is shear strength allowable in 12 plane;
F_{23} denotes the transverse shear strength;

Coefficient α (Table 3) computes how much is the contribution of the shear stress to the fiber tensile. Using $\alpha = 0$ and $F_{23} = \frac{F_{2c}}{2}$, the model represents the Hashin and Rotem (1973) criteria and using $\alpha = 1$, the model results in the model proposed in Hashin (1980). $\hat{\sigma}_{11}$, $\hat{\sigma}_{22}$ and $\hat{\sigma}_6$ are components of the effective stress tensor, from (21) (Lapczyk and Hurtado, 2007; Matzenmiller et al., 1995).

$$\hat{\boldsymbol{\sigma}} = \mathbf{M}\boldsymbol{\sigma} \tag{21}$$

where $\boldsymbol{\sigma}$ is the nominal stresses and $\mathbf{M}$ is the damage operator.

$$\mathbf{M} = \begin{bmatrix} \frac{1}{(1-d_f)} & 0 & 0 \\ 0 & \frac{1}{(1-d_m)} & 0 \\ 0 & 0 & \frac{1}{(1-d_s)} \end{bmatrix} \tag{22}$$

The parameters d_f, d_m and d_s are introduced to quantify the relative size, or, as also denoted, loss area and characterize fiber, matrix, and shear damage, corresponding to the four modes previously discussed. The compliance relationship is given, in terms of effective stress, by (23):

$$\boldsymbol{\epsilon} = \boldsymbol{H_0}\hat{\boldsymbol{\sigma}} \tag{23}$$

with

$$\boldsymbol{H_0} = \begin{bmatrix} \frac{1}{E_{||}} & -\frac{\upsilon_{21}}{E_{||}} & 0 \\ -\frac{\upsilon_{12}}{E_{\perp}} & \frac{1}{E_{\perp}} & 0 \\ 0 & 0 & \frac{1}{G} \end{bmatrix} \tag{24}$$

where $\boldsymbol{\epsilon}$ is the strain tensor and the parameters of the undamaged lamina $E_{||}$, $E_{\perp}$, G, υ_{12} and υ_{21} are, respectively, the Young's modulus in the fiber direction, Young's modulus in the direction perpendicular to the fibers, shear modulus and Poisson's ratios (for the Poisson's ratios, first subscript associates the loading direction and the second the direction of transverse strain).

Equations (21) and (23) results in (25):

$$\boldsymbol{\epsilon} = \boldsymbol{H_0 M \sigma} \tag{25}$$

Therefore, the damaged variables are related with undamaged variable as, for longitudinal Young's modulus:

$$E_1 = (1 - d_f)E_{||} \tag{26}$$

for transverse Young's modulus:

$$E_2 = (1 - d_m)E_{\perp} \tag{27}$$

and for shear modulus:

$$G_{12} = (1 - d_s)G \tag{28}$$

3.3.3. Filament winding

The filament winding manufacturing process, shown in Figure 11, consists of winding continuous fibers embedded in the resin through a rotating mandrel. Then, the mandrel is removed (demolding), giving the shape of the piece. This process is commonly used in the production of tubes (for transporting oil, for example), missiles, rockets, among other shell structures (Gay, 2015).

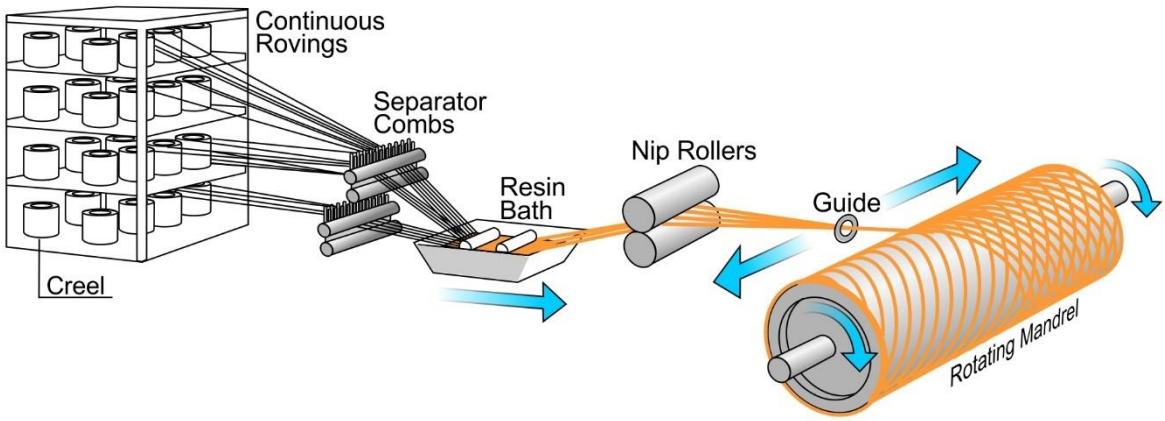

Figure 11: Illustration of filament winding process (Nuplex, 2018)

3.3.4. Pultrusion

The pultrusion process consists of pulling dry fibers, which are then impregnated with resin, through metal molds. The molds are generally heated, which accelerates curing of the resin

(Gay, 2015). Thus, it is possible to form continuous profiles (open or closed), as shown in Figure 12.

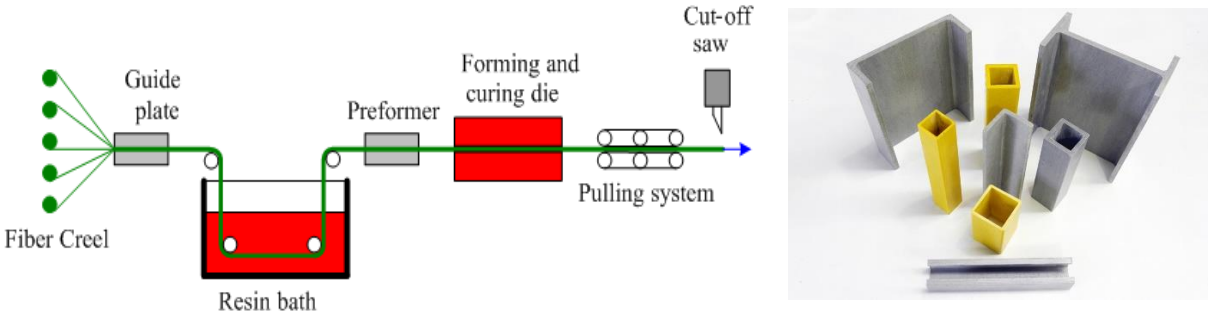

(a) (b)

Figure 12: (a) Pultrusion process (Kopeliovich, 2012) and (b) example of possible geometries (Core6, 2018)

3.4. Structural stability

According to Chen and Lui (1987), when the change in the geometry of a structure or the compression of a component results in the loss of the capacity to resist the loads, this condition is called structure instability. Such conditions can lead to catastrophic failures and should be considered in the design, especially in slender structures.

The inner rings and stringers of a semi-monocoque structure divide the structure into panels. For sufficiently rigid rings, a structure subjected to bending loads will usually fail in the side under compression, as shown in Figure 13a. In this case, the stringers act as columns. In another case, shown in Figure 13b, general instability may occur, which in other words is an extension of local buckling to the other panels, which may occur due to low stiffness of the rings (Niu, 1988).

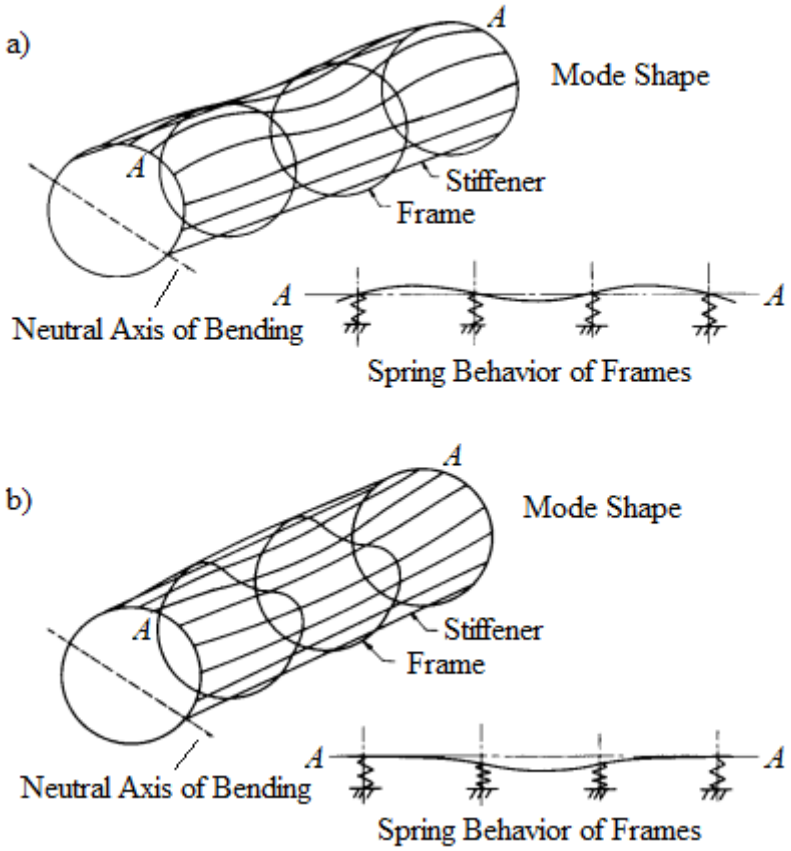

Figure 13: a) Modes shapes for panel and b) general instability of stiffened cylinders in bending (Adapted from Becker, 1958)

To solve simple cases of linear buckling, the analysis of eigenvalue is sufficient. In the eigenvalue problem, we look for the loads where stiffness matrix of the singular structure model has nontrivial solutions to:

$$\boldsymbol{K}^{MN}\upsilon^{M} = 0 \qquad (29)$$

where:

K^{MN} is the tangent stiffness matrix;

υ^{M} are nontrivial displacement solutions.

One of the steps of the solution is to apply an incremental load, Q^{N}, which is not important in its magnitude, since it will be scaled by the multiple λ_i, found in the eigenvalue problem, presented in (30), which estimates the critical buckling load (bifurcation) of the structure (Dassault Systèmes, 2014).

$$(\boldsymbol{K}_0^{NM} + \lambda_i \boldsymbol{K}_\Delta^{NM}) v_i^M = 0 \quad (30)$$

where:

$\boldsymbol{K}_0^{NM}$ is the stiffness matrix corresponding to the base state, which includes the effects of the preloads;

$\boldsymbol{K}_\Delta^{NM}$ is the differential initial stress and load stiffness matrix due to the incremental loading pattern;

λ_j are the critical buckling (eigenvalues);

v_j^M are the buckling mode shapes (eigenvectors);

M e *N* refer to degrees of freedom *M* and *N* of the whole model;

j refers to the *j*th buckling mode.

When material nonlinearity and geometric nonlinearity should be considered in buckling, or unstable post buckling response, load-deflection using a Riks method analysis can be performed to investigate the problem. This method can be used with the introduction of an initial imperfection in the "perfect" geometry of the structure. These imperfections are introduced by perturbations in geometry, from the buckling modes obtained in the linear analysis of buckling, that is, the process is done following an analysis of eigenvalues. More detailed information can be found in Abaqus™ manual (Dassault Systèmes, 2014).

4

METHODOLOGY

4.1 Pole details

Figure 14 shows a pole illustration, with its main components depicted. The outer skin is an element that resists mainly shear and can be manufactured by filament winding. The longitudinal stringers (cross section shown in Figure 15b) are produced by pultrusion method and resist mainly axial and bending loads. The rings (Figure 15a) can be obtained cutting tubes produced by the filament winding process, according to the presented by Alves (2006). In this case, the fibers are positioned to 90° with the longitudinal tube axis. The rings have the purpose of stiffening the pole due to cross section ovalization. The skin, stringers and rings are made with GFRP. Material constitutive properties for the GFRP composite were obtained from Fam et al. (2010), presented in Table 4. The fiber volume fraction is 0.58.

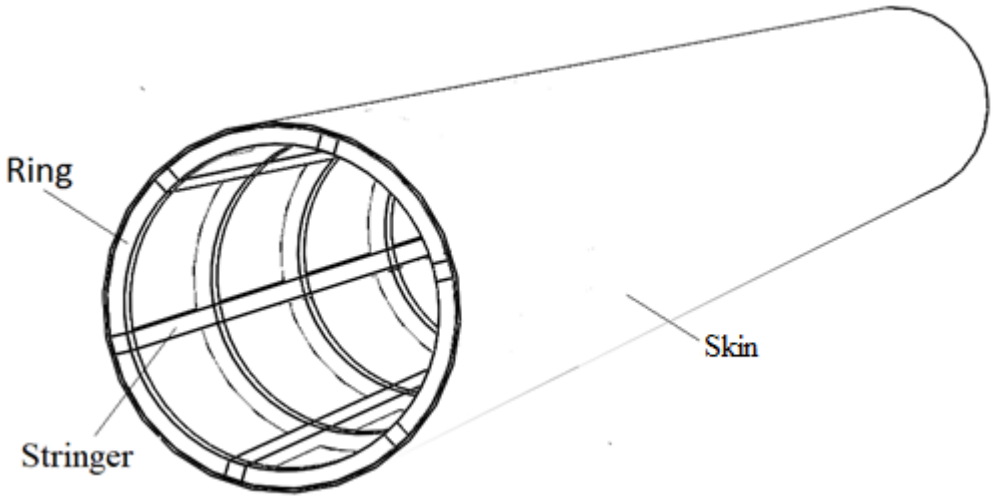

Figure 14: Illustration of the pole (elaborated by the author)

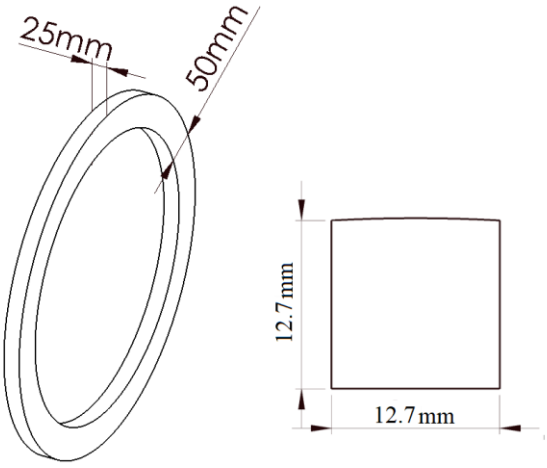

(a) (b)

Figure 15: Illustration of (a) rings and (b) stringers cross sections geometries

Table 4: GFRP mechanical properties (Fam et al., 2010)

E_1 (MPa)	E_2 (MPa)	ν_{12}	G_{12} (MPa)	F_{1t} (MPa)	F_{1c} (MPa)	F_{2t} (MPa)	F_{2c} (MPa)	F_{12} (MPa)
43300	11900	0.24	4600	1020	620	40	140	60

The geometry and load, shown in Figure 16, are based in CEMIG (2010). The diameters of the base and the top of the pole are respectively 350 mm and 170 mm, while the total height is 12 m, with 1.8 m of grounding. The maximum deflection allowed at the top is five per cent of the nominal length when the load of 3000 N is applied horizontally at 100 mm bellow the top (CEMIG, 2010).

In this work, as mentioned previously, the behavior of four different pole configurations are analyzed and designated as A, B, C and D. The numbers of rings and stringers were investigated as structural members to evaluate their effects on strength and mass. Table 5 presents the configurations to be evaluated.

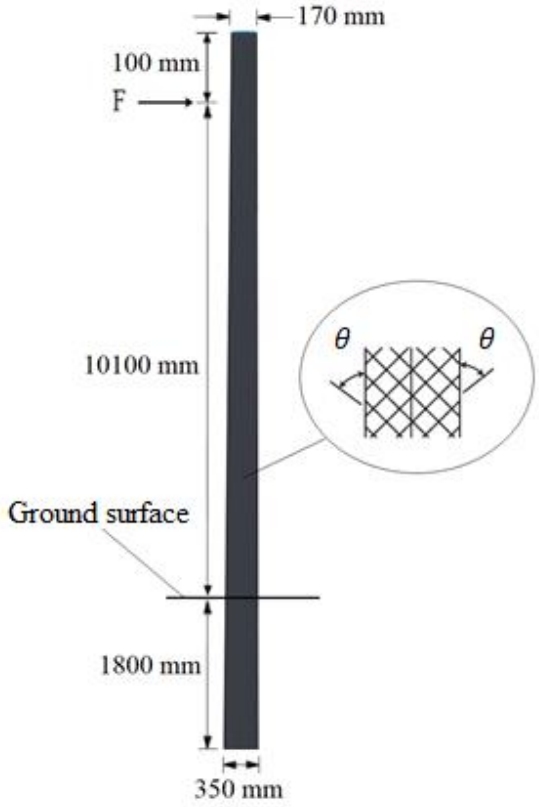

Figure 16: Pole geometry

Table 5: Number of stringers and rings analyzed

Condition	Stringers	Rings
A	Without	Without
B	Investigated	Without
C	Without	Investigated
D	Investigated	Investigated

4.2. Numerical model

The finite difference method is relatively simple to apply when compared to finite element methods (FEM). To conform the maximum deflection allowed at the top (five per cent of the nominal length) and analyze the behavior when the fiber angles changes, the code developed by Alípio (2014) based in the finite difference method is adopted and used in this work to verify the deflection, when the required load is applied. Then, the FEM analysis are conducted.

The finite element method has been a widely used tool to determine product behavior, which can help reduce costs and reduces the possibility of problems in prototypes. In this work the FEM, through commercial software Abaqus™, is used in order to determine the behavior of the pole, using progressive failure analysis for composite materials. The Riks method is used not

only to predict the failure behavior of the material, but also the non-linear buckling behavior. The Hahin Failure criteria is used, taking $\alpha = 0$ and $F_{23} = \frac{F_{2c}}{2}$ (Hashin and Rotem, 1973). In the Riks method, the imperfections were introduced as superposition of buckling eigenmodes obtained from linear buckling. The damage initiation at a material point, according Hashin criteria, is identified in Abaqus™ through the variables HSNFTCRT, HSNFCCRT, HSNMTCRT and HSNMCCRT, where (DASSAULT SYSTÈMES, 2014):

HSNFTCRT - Maximum value of the fiber tensile initiation criterion experienced;
HSNFCCRT - Maximum value of the fiber compressive initiation criterion experienced;
HSNMTCRT - Maximum value of the matrix tensile initiation criterion experienced;
HSNMCCRT - Maximum value of the matrix compressive initiation criterion experienced.

The model generated in Abaqus™ is shown in Figure 17. The skin is modelled with SR4 shell elements, which consists of four nodes and reduced integration number, with six degrees of freedom at each node. For the stringers and rings, the B31 beam elements are also used, with six degrees of freedom at each node. The degrees of freedom in *x, y* and *z* axes system correspond to the *1*, *2* and *3* local axes, respectively. The model is restrained in all the degrees of freedom (U1 = U2 = U3 = 0 and UR1 = UR2 = UR3 = 0) at a height of 1.8 m from the base, which corresponds to the ground level. To conduct the progressive failure, a displacement is applied horizontally at 100 mm bellow the top, in a referent point at center of the cross section, connected by rigid element.

In order to evaluate the quality of the finite element models, it was proposed the modelling of three experimental problems of the literature. The first consisted of the four-point test of a tube, the second and the third are tests of a monocoque cantilevered poles with lateral loading. The analyses are presented below.

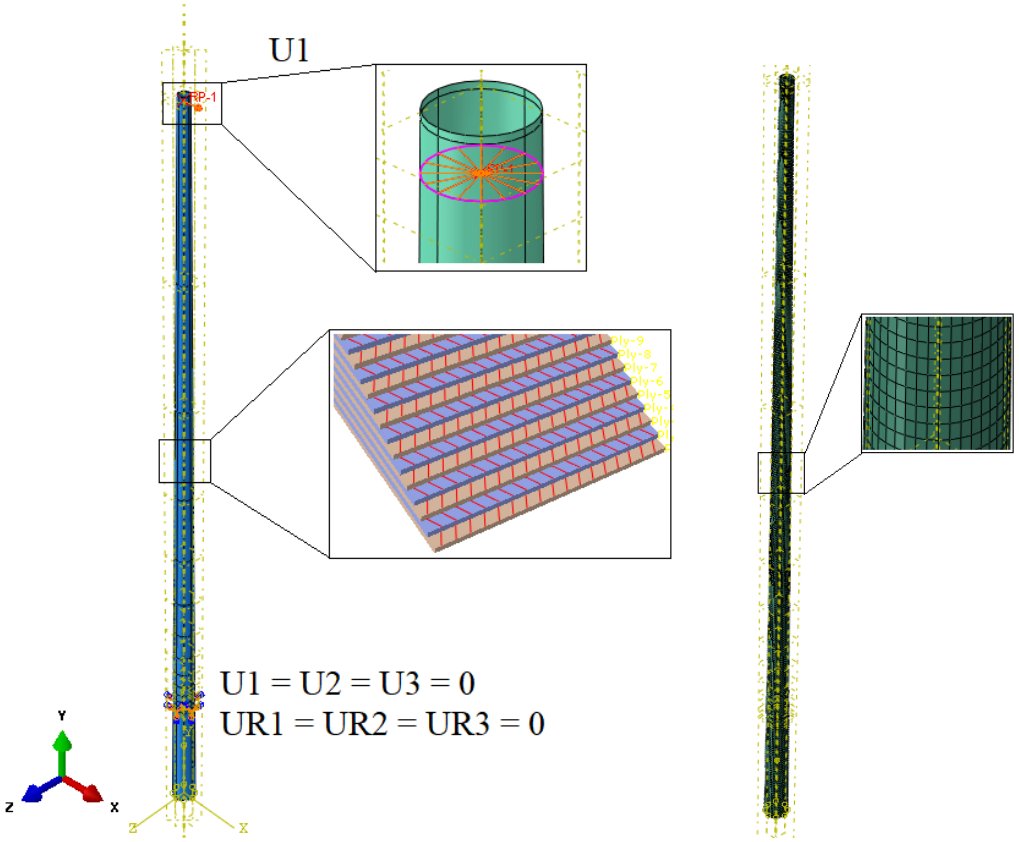

Figure 17: Abaqus™ model a) boundary conditions and b) mesh

4.2.1 Problem 1: Four-point test

Fam (2000) and his group conducted tests on composite tubes for use on structural members. One configuration of the model studied is shown in Figure 18 and consists of a 100 mm outer diameter GFRP tube with thicknesses and layup shown in Table 6. The four-point test consisted of applying the load in two regions of the tube, separated by 200 mm, under two supports separated by 1300 mm. The load was captured by a load cell shown in Figure 18 and the displacement was measured at the bottom of the center of the tube. The mechanical properties shown in Table 7 were obtained from Fam et al. (2010).

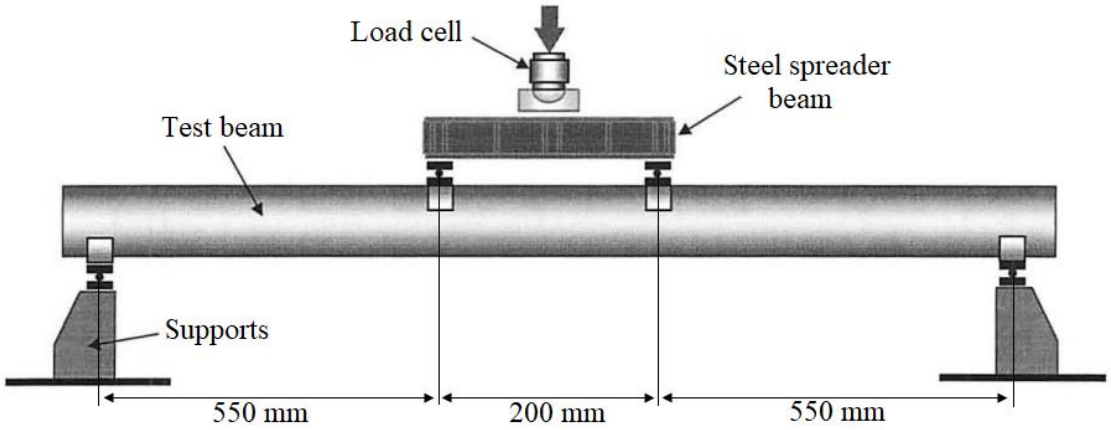

Figure 18: Four-point test (adapted from Fam, 2000)

Table 6: Thickness and orientation of each layer (Fam, 2000)

Thickness (mm)	0.32	0.35	0.27	0.48	0.26	0.51	0.19	0.51	0.19
Orientation	-88°	+3°	-88°	+3°	-88°	+3°	-88°	+3°	-88°

Table 7: Mechanical properties (Fam et al., 2010)

E_1 (MPa)	E_2 (MPa)	ν_{12}	G_{12} (MPa)	F_{1t} (MPa)	F_{1c} (MPa)	F_{2t} (MPa)	F_{2c} (MPa)	F_{12} (MPa)
38000	7800	0.28	3500	795	533	39	128	89

As the test conditions are symmetrical, only half of the tube was modeled. The boundary conditions are shown in Figure 19. A displacement was applied vertically in a referent point, connecting, by rigid element, the reference point and the nodes of the mesh. The model mesh is presented in Figure 20.

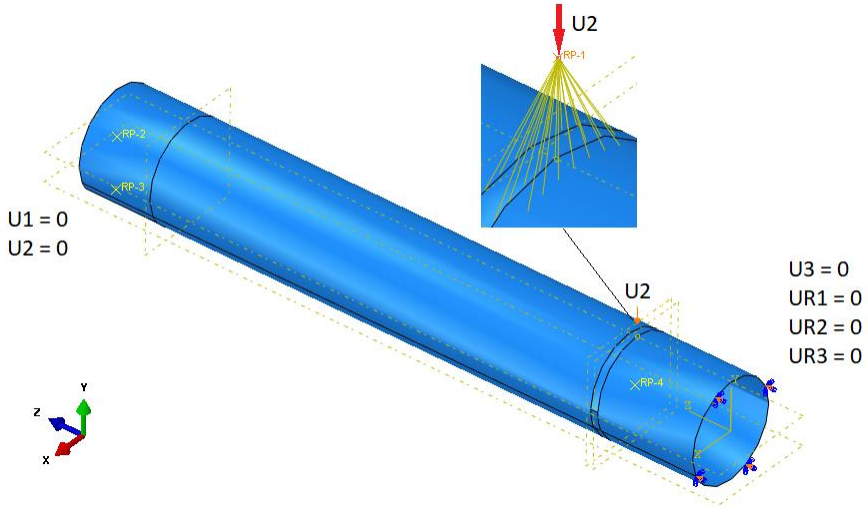

Figure 19: Boundary conditions

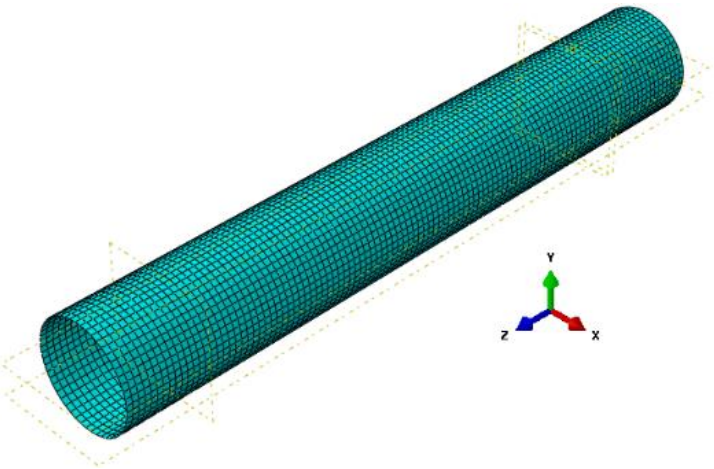

Figure 20: Mesh of the model

Figure 21 shows the results for the damaged tube. The material failure obtained was detected near the region where the load was applied and main failure mode was matrix compression. Figure 22 shows the load-displacement behavior, where the FEM model is compared with analytical stiffness (slope of the curve obtained through beam theory) and experimental results. The numerical analysis shows great agreement between analytical stiffens and experimental results.

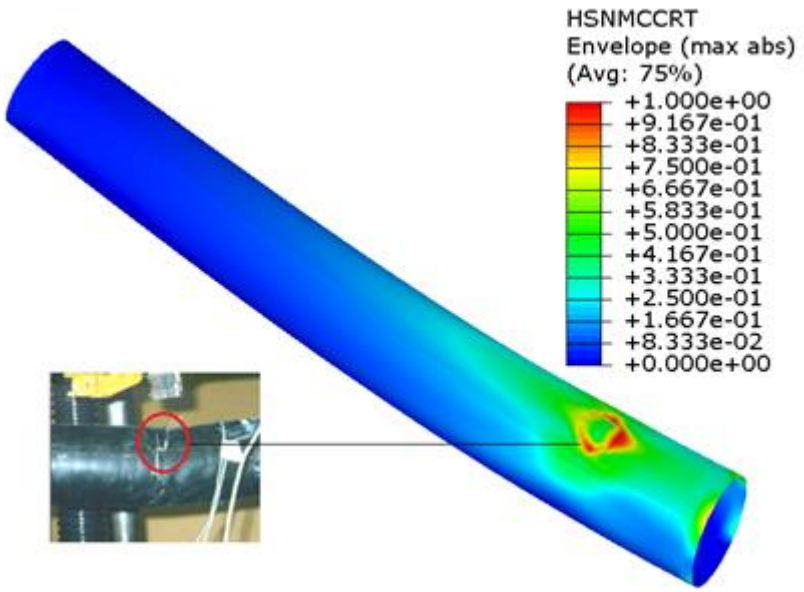

Figure 21: FEM results for matrix compression of Hashin criteria compared with Fam (2000) results.

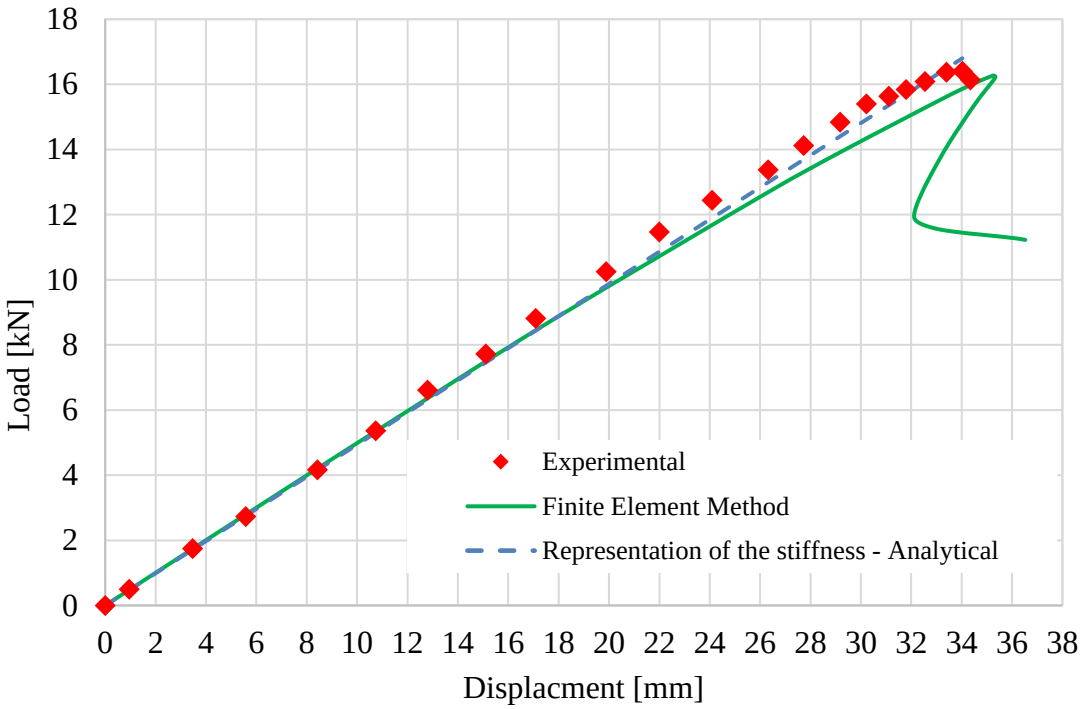

Figure 22: Load-displacement behavior for problem 1

4.2.2 Problem 2: Cantilevered pole test

The second problem was one specimen of the experimental program conducted by Ibrahim (2000) - mentioned in the literature review. The GFRP monocoque pole was tapered hollow 2.5 m in length and the inner diameters at base and top were, respectively, 100 mm and 74 mm. Ten layers oriented at 35º/-35° with the longitudinal axis were used. The total wall thickness at base was 2.2 mm. The geometry is represented in Figure 23, and Table 8 provides the mechanical properties of the GFRP. Figures 24a and 24b show the mesh and the boundary conditions respectively.

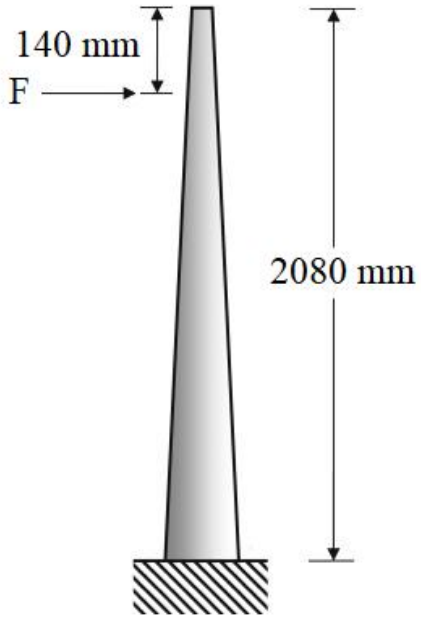

Figure 23: Geometry illustration

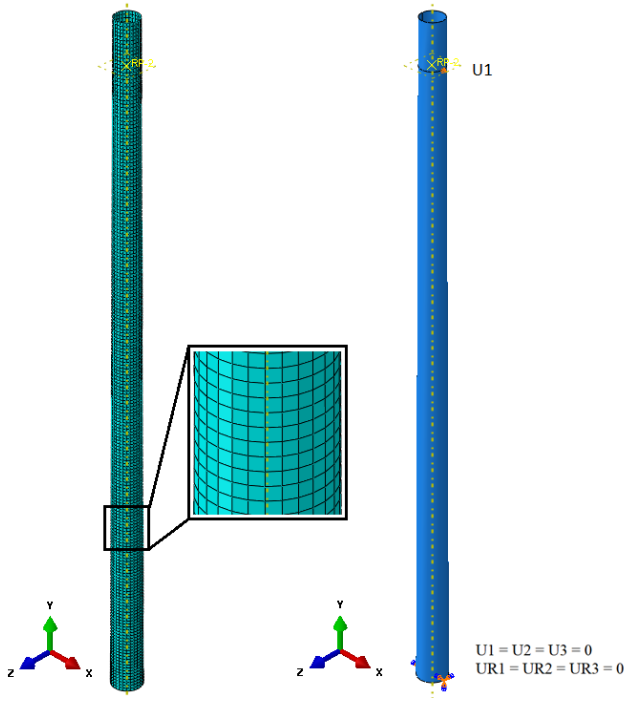

a) b)

Figure 24: a) Mesh and b) boundary conditions for the problem 2

Figure 25 shows the FEM results for maximum matrix compression index that represent the material failure near the base. Figure 26 shows good agreement between the results when FEM is compared with experimental and the representation of the stiffness.

Table 8: Mechanical properties of the GFRP (Ibrahim, 2000)

E_1 (MPa)	E_2 (MPa)	ν_{12}	G_{12} (MPa)	F_{1t} (MPa)	F_{1c} (MPa)	F_{2t} (MPa)	F_{2c} (MPa)	F_{12} (MPa)
44600	12460	0.24	4850	1300	691	47	130	44

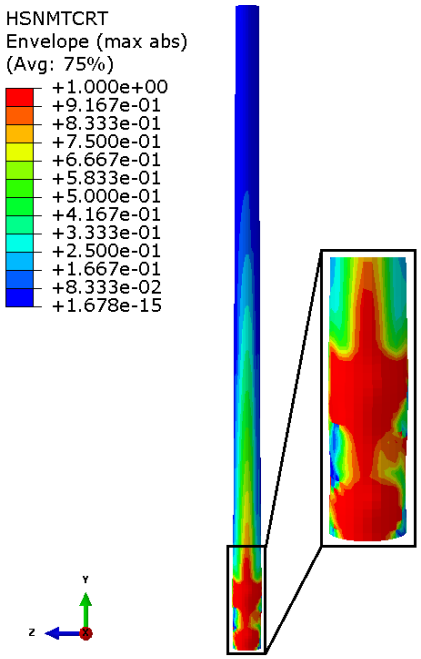

Figure 25: Failure analysis where the matrix tensile index is show

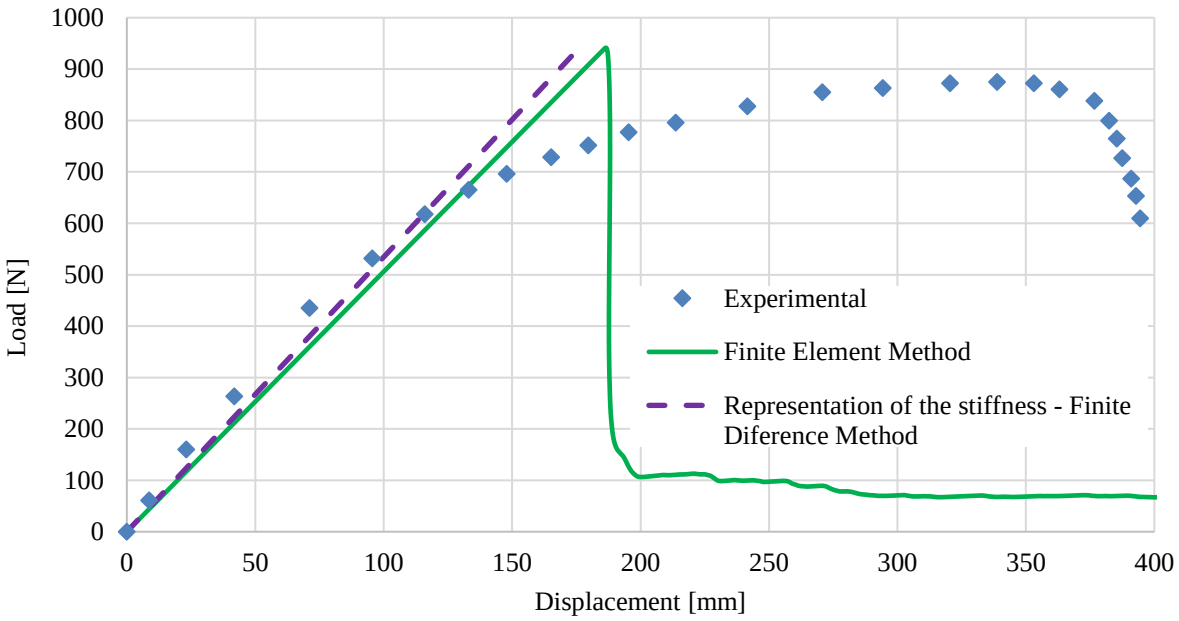

Figure 26: Load-displacement behavior for problem 2

4.2.3 Problem 3: Cantilevered pole test with buckling behavior

The third problem was another specimen of the experimental program conducted by the same author, Ibrahim (2000). The geometry and material mechanical properties of GFRP were the same presented in problem 2. However, for this specimen, four layers oriented at 25º/-25° with the longitudinal axis were used. The total wall thickness at base was 0.88 mm. The illustration of mesh and boundary conditions are represented in Figures 27a and 27b, respectively.

Figure 28 shows the buckling behavior of the pole analyzed. In this case, the model presented a local instability near the base, before the material failure, leading to loss of stiffness. The buckling occurred due to a very thin wall thickness. The load-displacement behavior is represented in Figure 29. The nonlinear simulation via FEM had good agreement with

experimental results. However, as the FDM is a linear method, the linear behavior had a good agreement, with small divergence in the non-linear part.

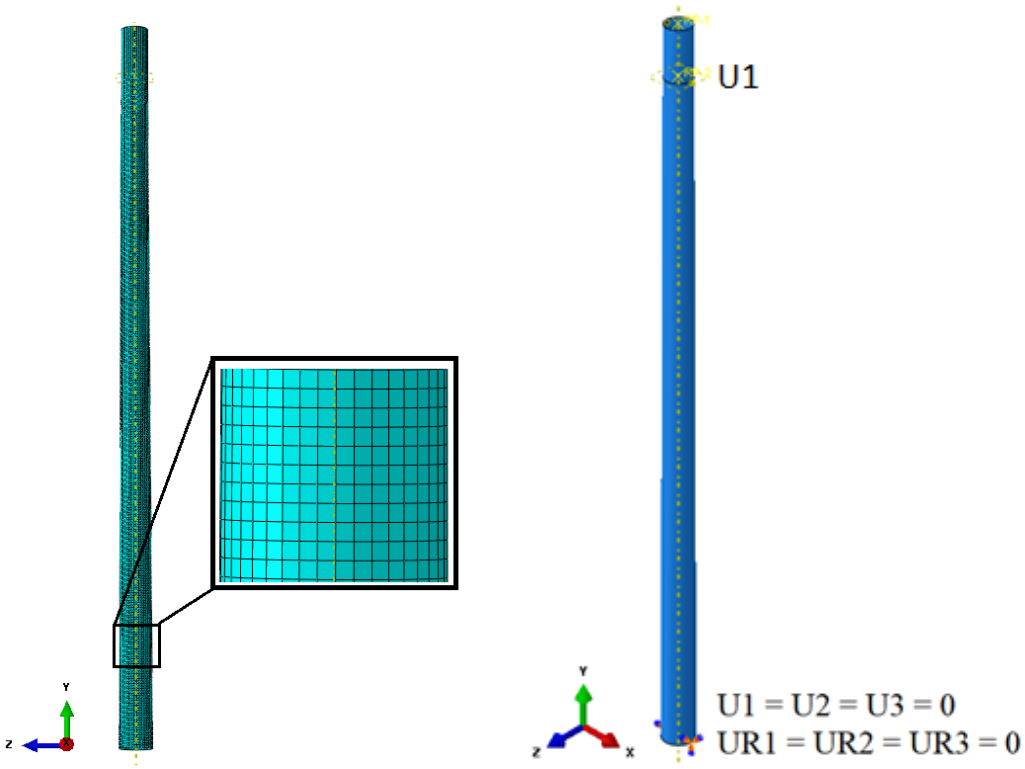

a) b)

Figure 27: a) mesh and b) boundary conditions for problem 3

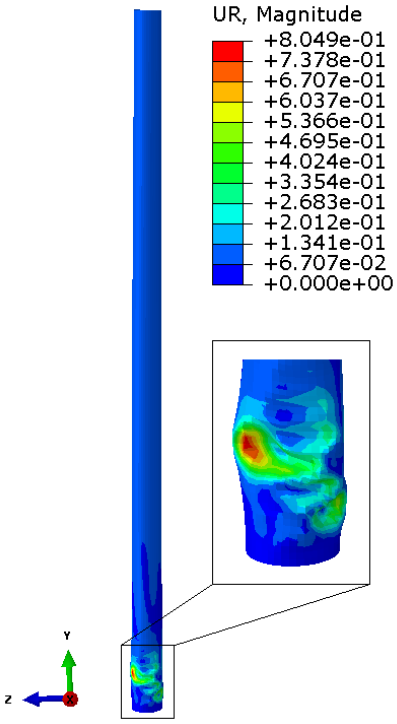

Figure 28: Failure analysis for problem 3 where the magnitude of nodal rotations UR highlights the local buckling failure

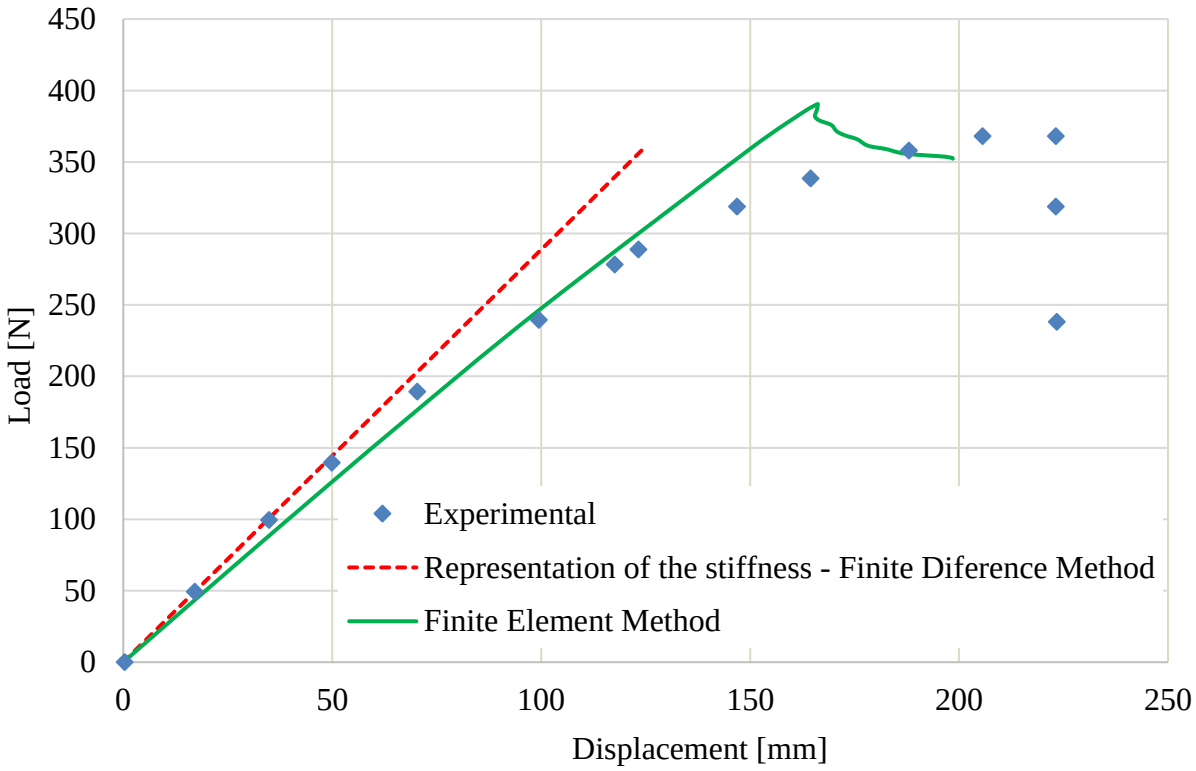

Figure 29: Load-displacement behavior for problem 3

5

RESULTS AND DISCUSSIONS

5.1 Parametric analysis

Using FDM, a parametric study was conducted to analyze the best pole configurations and the effects of the stringers. The longitudinal angle of the fibers was varied for the conditions of load and stiffness (maximum deflection) mentioned in the methodology. First this process was done for the monocoque pole, then the stringers were added. For each angle of the fibers (ranging from 10 ° to 10 °) and number of stringers, the number of layers of the skin was determined so that the maximum resulting deflection to be equal to or immediately below 5% of the pole length, for purposes of comparison. Thus, the angles of the fibers were plotted as a function of thickness, mass and number of stringers. Figures 30 and 31 show the results as a function of the thicknesses and masses, respectively. To compute the mass, was considered $\rho = 1.94$ g/cm³ (Ibrahim, 2000).

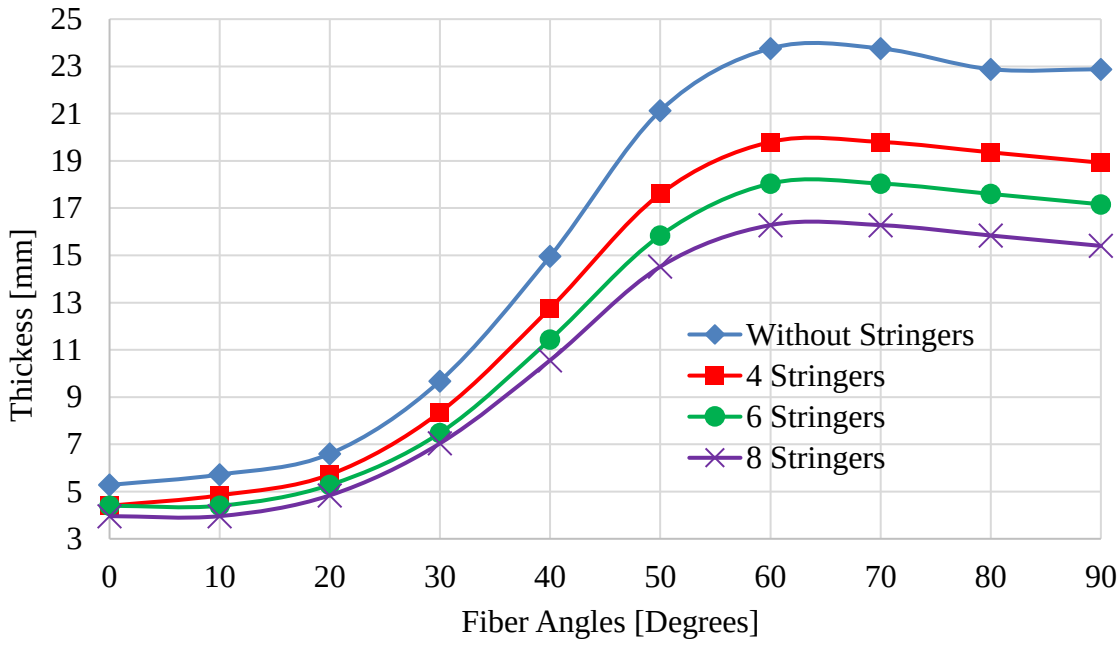

Figure 30: Effects of stringers and fiber angles on the thickness

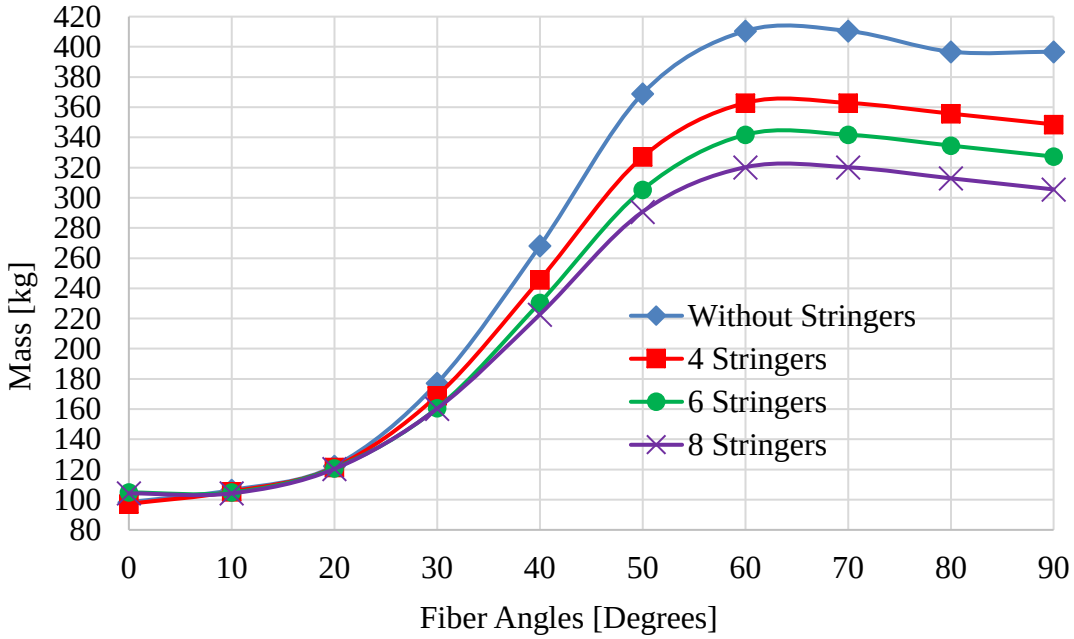

Figure 31: Effects of stringers and fiber angles on the mass

It can be noted that for small angles, the thickness, and consequently the resulting mass, does not vary greatly from one configuration to another. However, for larger angles, there is a large difference between the thicknesses and the masses. This behavior is due to the fact that the longitudinal stiffness can be increased when the angle of the fibers is close to the angle of the pole (smaller angles) and, in the case of larger angles, the stringers have great effect, since they have fiber angles at 0 °. In Figures 30 and 31, the pole without stringers corresponds to pole A and the pole with eight stringers corresponds to the pole B. Pole C has the same configuration as pole A, but with rings. Pole D has the same configuration of Pole B, adding rings and stringers.

Many manufacturing processes by filament winding have restrictions for low thicknesses and angles very close to the longitudinal pole angle. Therefore, for FEM analysis, it was decided to analyze poles with angles of ±30 ° symmetrically balanced. According to parametric analysis, for conditions with stringers, eight stringers were used due to lower mass. For conditions with rings, the spacing and number of rings were based on linear buckling modes. Therefore, fifteen rings were added according a geometric sequence of ratio 1.36, starting at ground line surface with 50 mm in first spacing. Table 9 shows the details of layers and deflection obtained, for a load of 3000 N.

Table 9: Number of layers, thickness and maximum deflection for 3000 N of load, obtained on parametric study

Condition	Nº Layers	Skin thickness (mm)	Maximum deflection (% of the total length)
A	44	9.68	4.89
B	32	7.04	4.81
C	44	9.68	4.89
D	32	7.04	4.81

The masses of each configuration and the contribution of each structural element are presented in Figures 32 and 33.

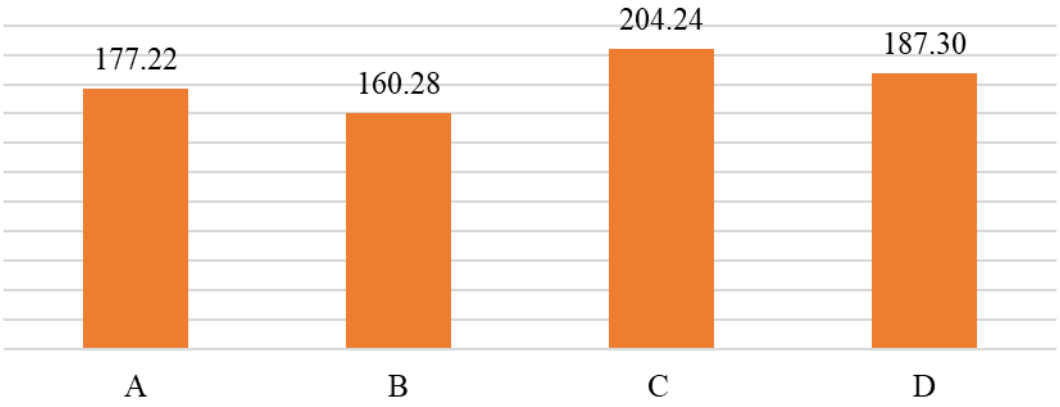

Figure 32: Mass (kg) obtained for each pole

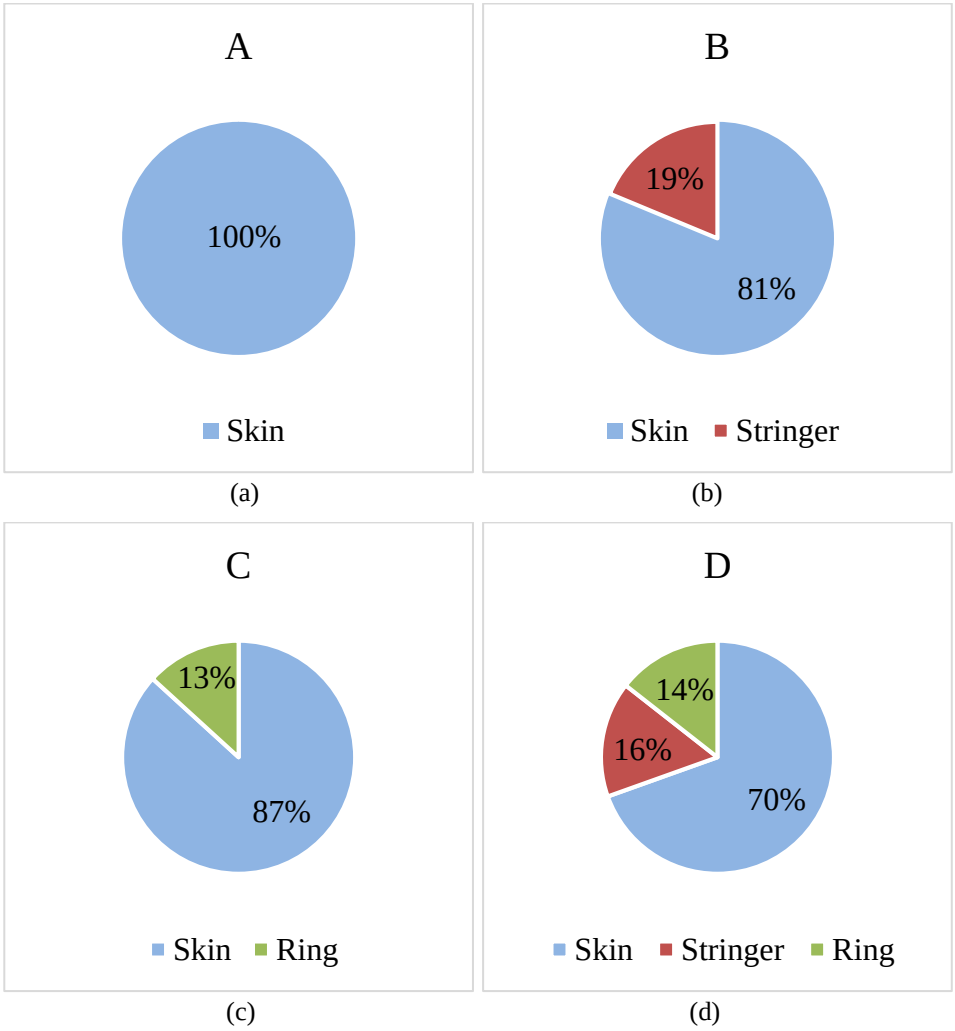

Figure 33: Contribution of each structural item in the pole mass

5.2. Pole A - monocoque

The analysis for the monocoque model (configuration A) was then conducted. The resulting load-displacement curve is shown in Figure 34. It can be observed a close proximity of the stiffness of the FEM model in the linear region when compared with FDM model. To analyze the failure along the curve, four points were identified in the graphs and analyzed. For each point, the four failure modes in the region most susceptible to failure were analyzed. In the first point (Figure 35), corresponding to a displacement of 5 % of the total pole length, it is noted that there is no failure for the analyzed modes. For the second point (Figure 36), the maximum load, corresponding to 14.04 kN, is reached. Failure occurs in the region of the pole subject to compression, for the matrix tensile mode. In this case, the fibers are compressed and cause matrix tensile. In the third point (Figure 37) there is a progression of failure, where it is

identified, besides the matrix tensile failure, failure in the matrix compression mode. At point four (Figure 38) the pole has already lost the capacity to support load and begins to fail in the fiber compression mode. For all the cases, there is no failure in fiber tensile.

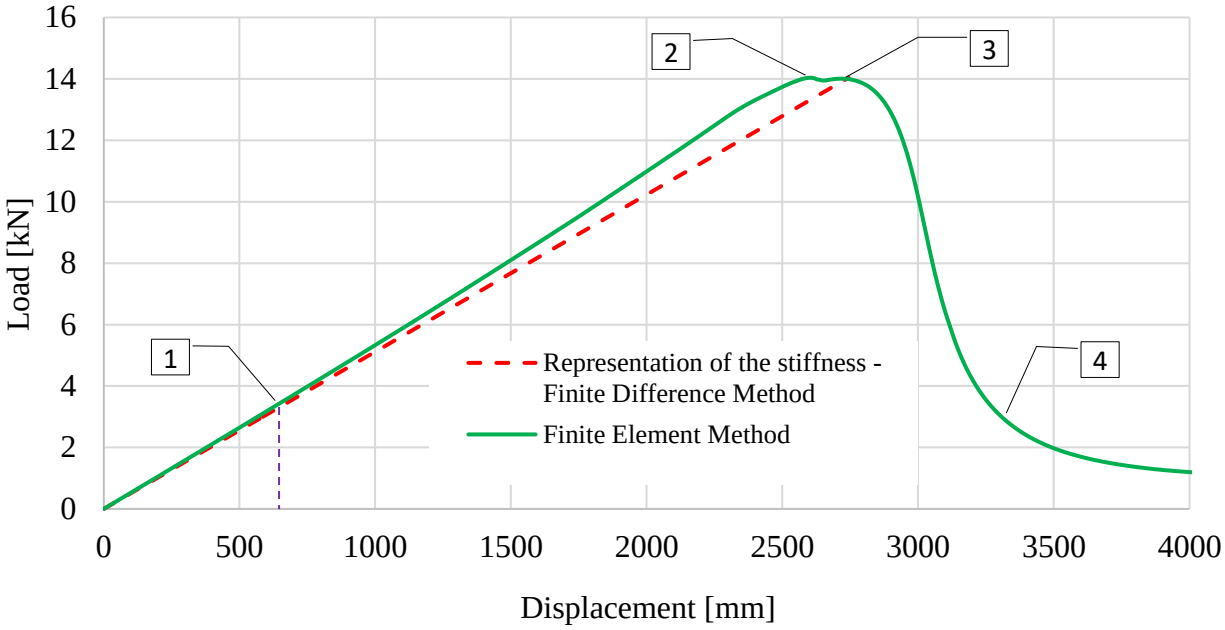

Figure 34: Behavior of pole A

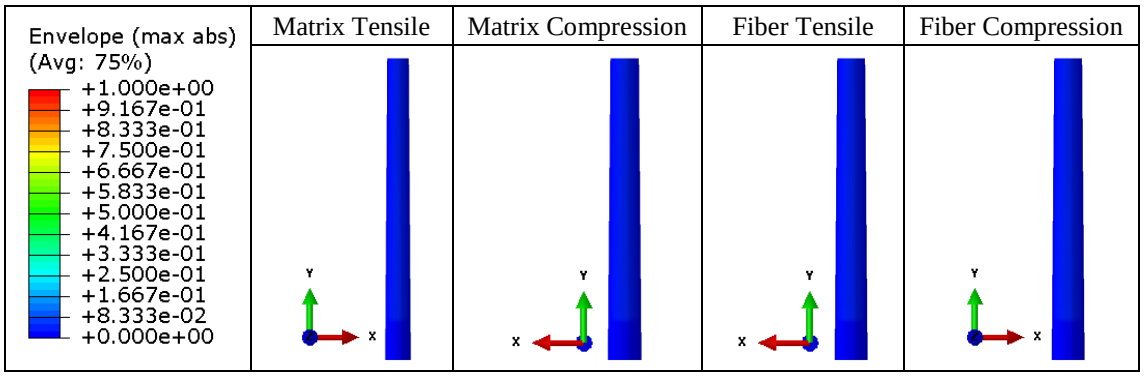

Figure 35: Values of the damage initiation criterion experienced during the analysis for point 1 of Figure 34

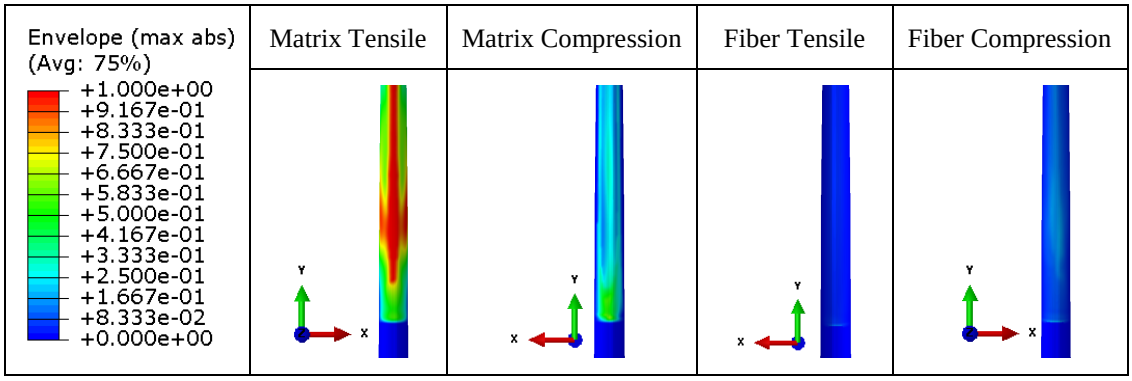

Figure 36: Values of the damage initiation criterion experienced during the analysis for point 2 of Figure 34

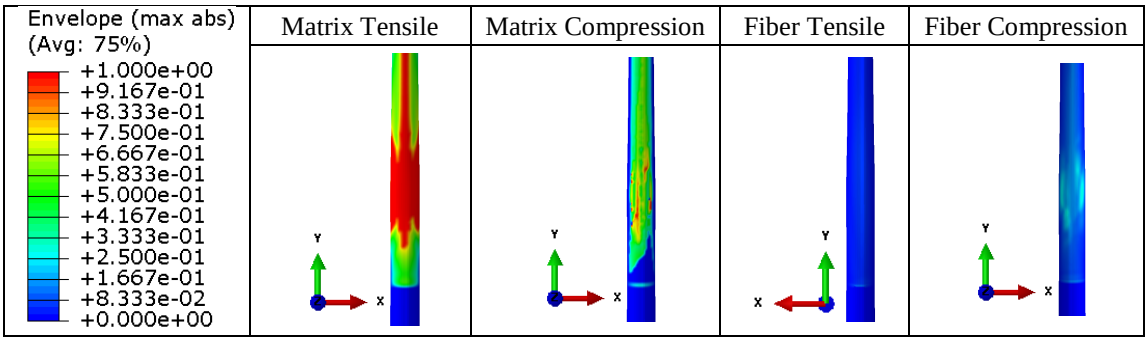

Figure 37: Values of the damage initiation criterion experienced during the analysis for point 3 of Figure 34

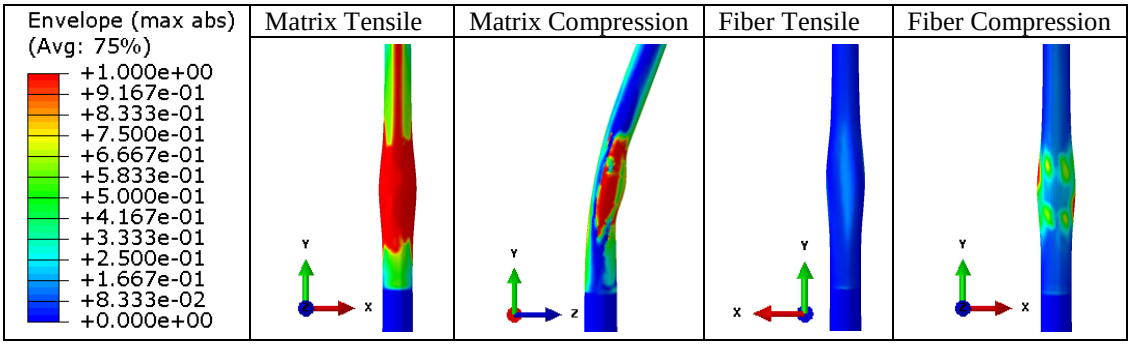

Figure 38: Values of the damage initiation criterion experienced during the analysis for point 4 of Figure 34

5.3. Pole B – semi-monocoque with stringers

The pole with longitudinal stringers (Pole B) load-displacement behavior is shown in Figure 39. There was a good agreement of the FEM model stiffness when compared to the FDM model. Three points were taken to analyze the failure. For this case, the simulation was conducted until point three, where it was identified a stress that would lead to the stringer failure. This process was done due the damage model is applied specifically to the shell. In the first point, corresponding to a deflection of 5 % of the total pole length, there is no failure (Figure 40). The second point reaches the maximum load of 11.58 kN and matrix tensile failure occurs on the compressed side (Figure 41). In the third point, there is an evolution of the matrix tensile failure and the beginning of matrix compression failure. It is also verified, by analyzing the normal stress, that the most compressed stringer reaches the maximum material failure stress in the compression side in the fiber direction (Figure 42).

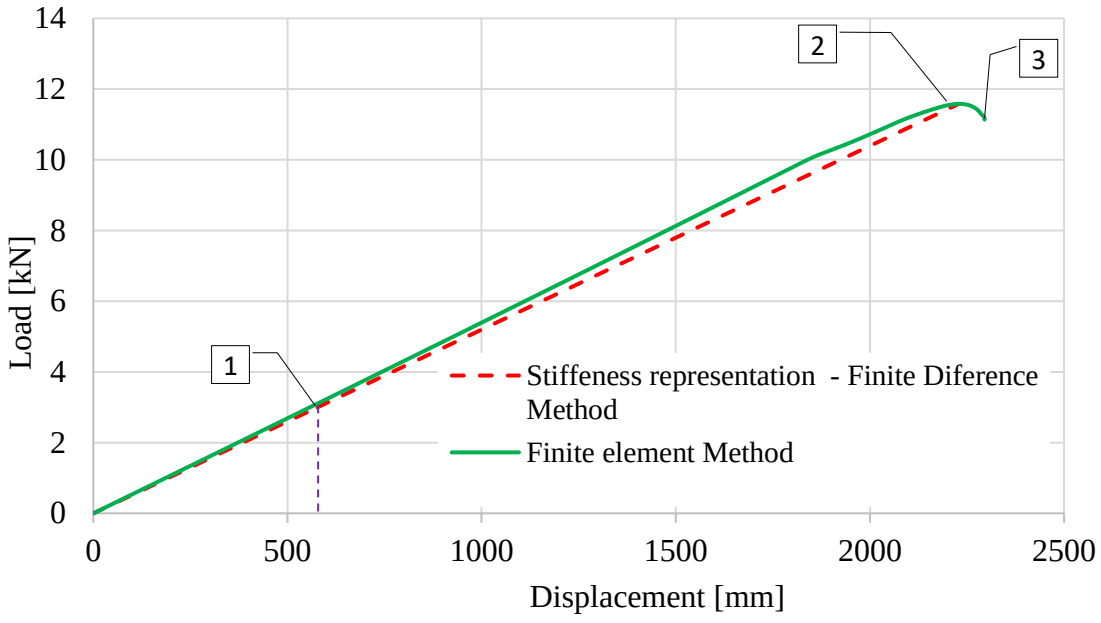

Figure 39: Behavior of Pole B

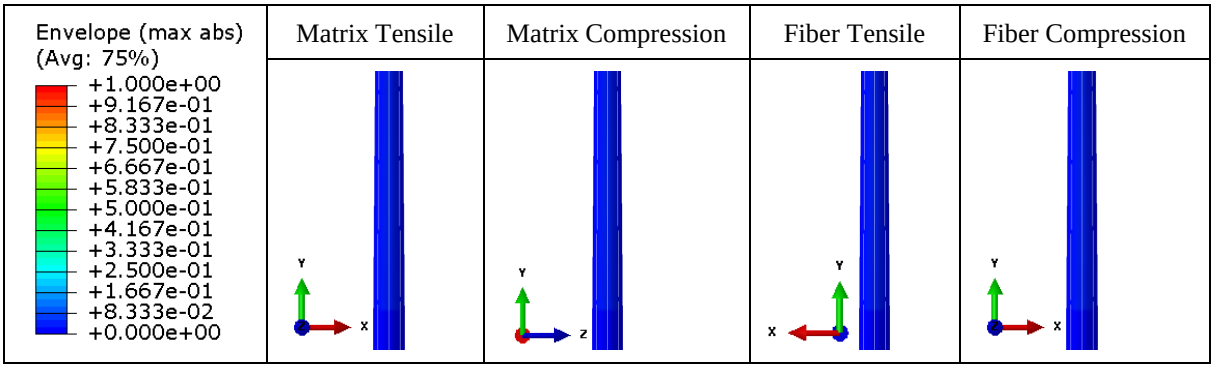

Figure 40: Values of the damage initiation criterion experienced during the analysis for point 1 of Figure 39

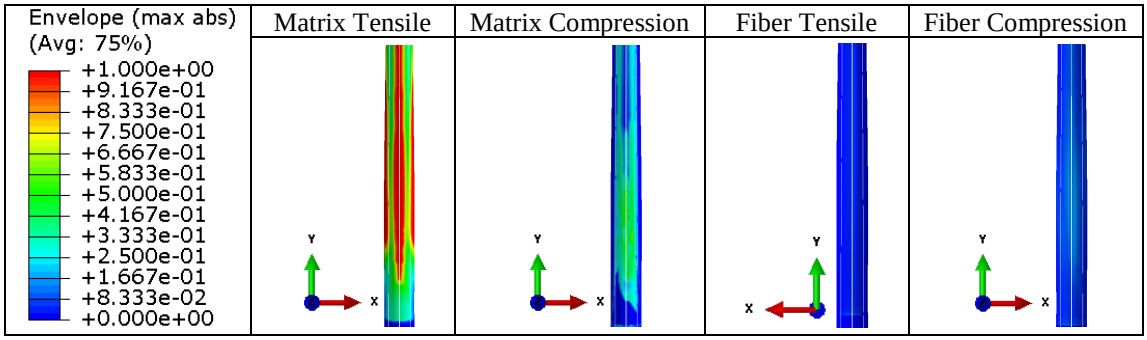

Figure 41: Values of the damage initiation criterion experienced during the analysis for point 2 of Figure 39

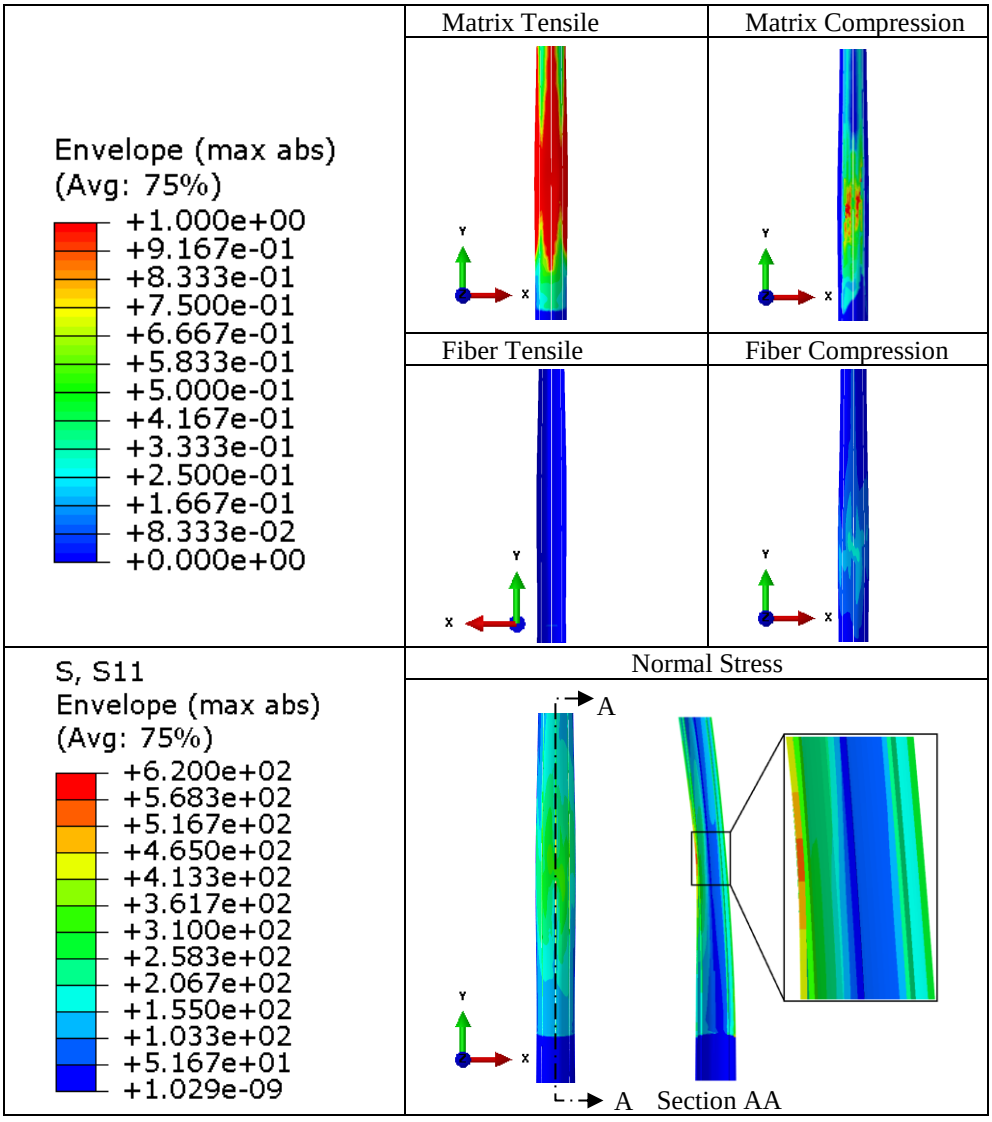

Figure 42: Values of the damage initiation criterion experienced during the analysis for point 3 of Figure 39

5.4. Pole C – semi-monocoque with rings

For the configuration C, with rings and without longitudinal stringers, the pole load-displacement behavior is shown in Figure 43. For small displacements, there was a good agreement of the FEM model stiffness when compared to the FDM model. Three points were taken to analyze the failure. In the first point, corresponding to a deflection of 5 % of the total pole length, there is no failure (Figure 44). The second point reaches the maximum load of 16.84 kN and, as the pole A and B, matrix tensile failure occurs on the compressed side (Figure 45), between the rings. In the third point, the pole section lost the capacity to resist the loads

(Figure 46), which caused the load fall. At this point, there is also a failure for the matrix compression and fiber compression.

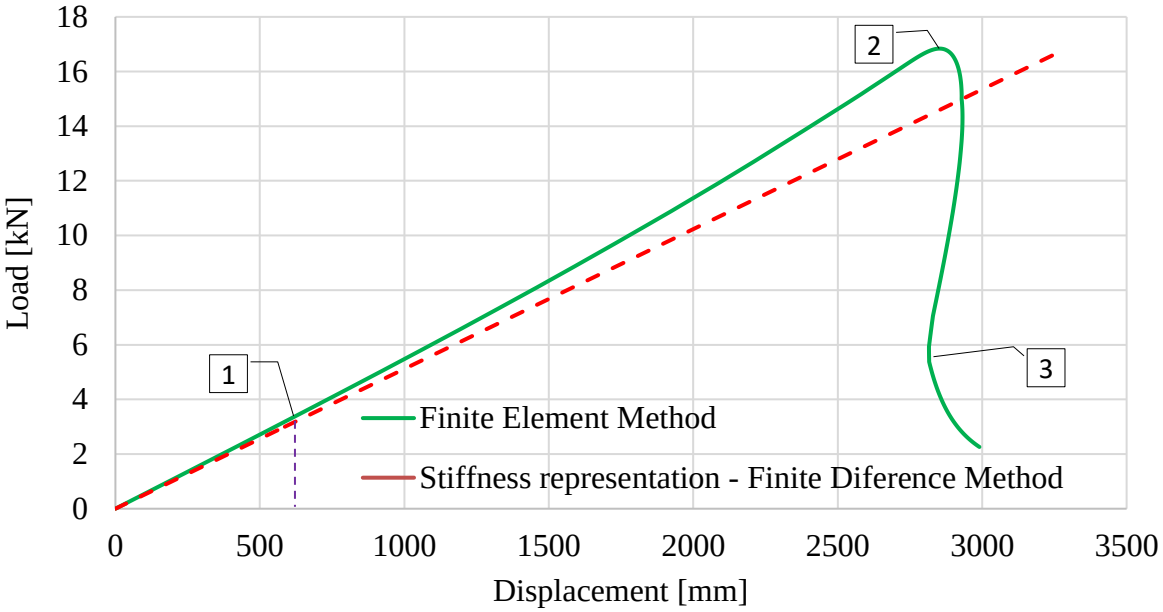

Figure 43: Behavior of pole C

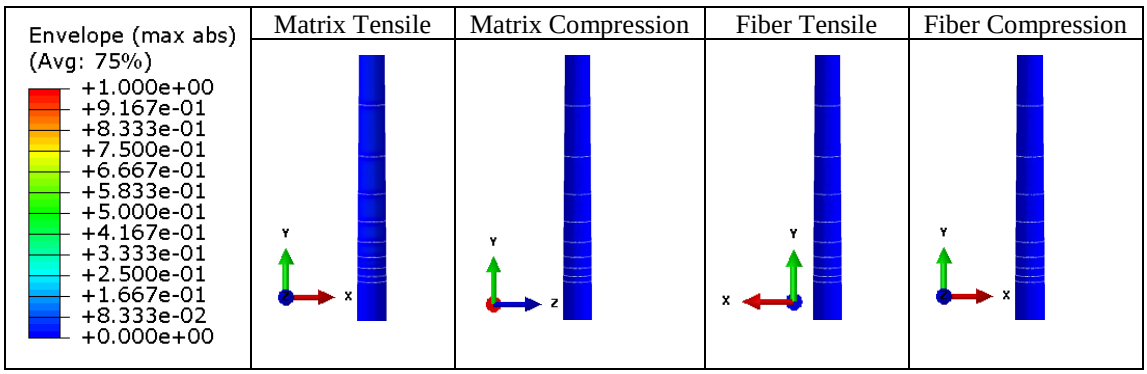

Figure 44: Values of the damage initiation criterion experienced during the analysis for point 1 of Figure 43

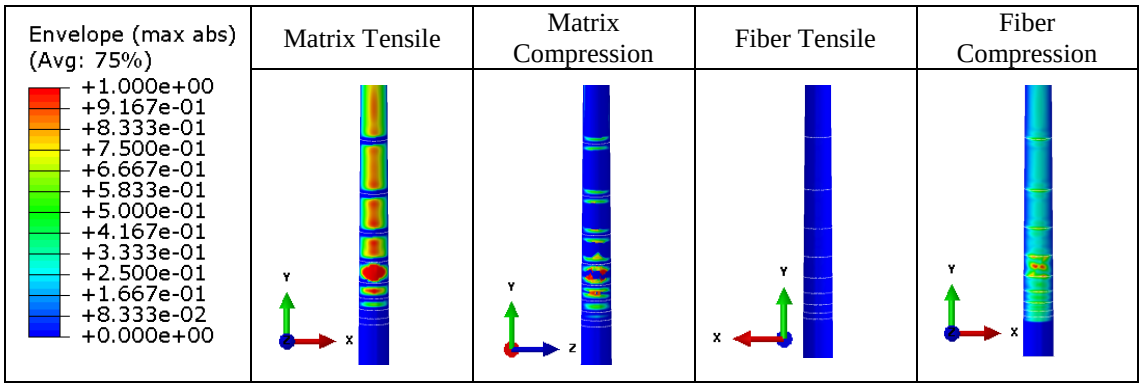

Figure 45: Values of the damage initiation criterion experienced during the analysis for point 2 of Figure 43

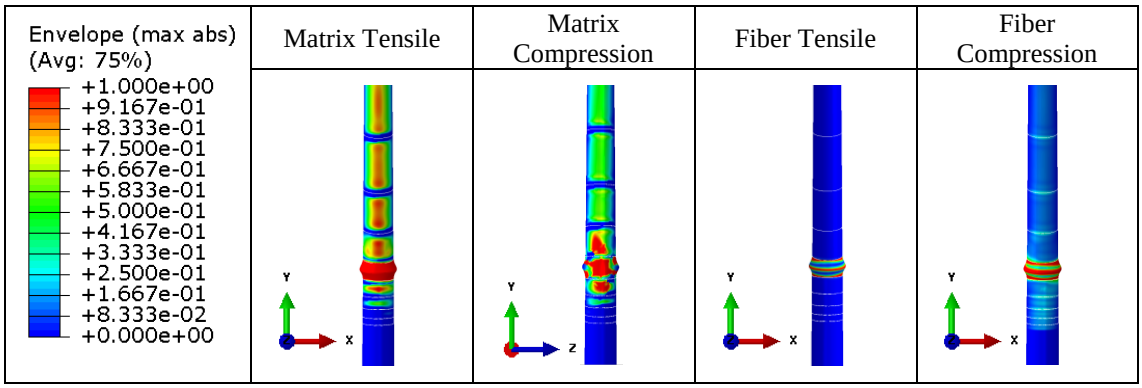

Figure 46: Values of the damage initiation criterion experienced during the analysis for point 3 of Figure 43

5.5. Pole D – semi-monocoque with stringers and rings

The configuration D, with longitudinal stringers and rings, presented the load-displacement behavior shown in Figure 47. There was a good agreement of the FEM model stiffness and FDM model. Two points were taken to analyze the failure. For the deflection corresponding to 5 % of the total pole length (point 1), there is no failure (Figure 48). The second point reaches the maximum load of 16.29 kN. In this point, the stringer presented the maximum stress strength

on the compressed side (Figure 49), between the rings and there is also a failure for the matrix tensile and matrix compression.

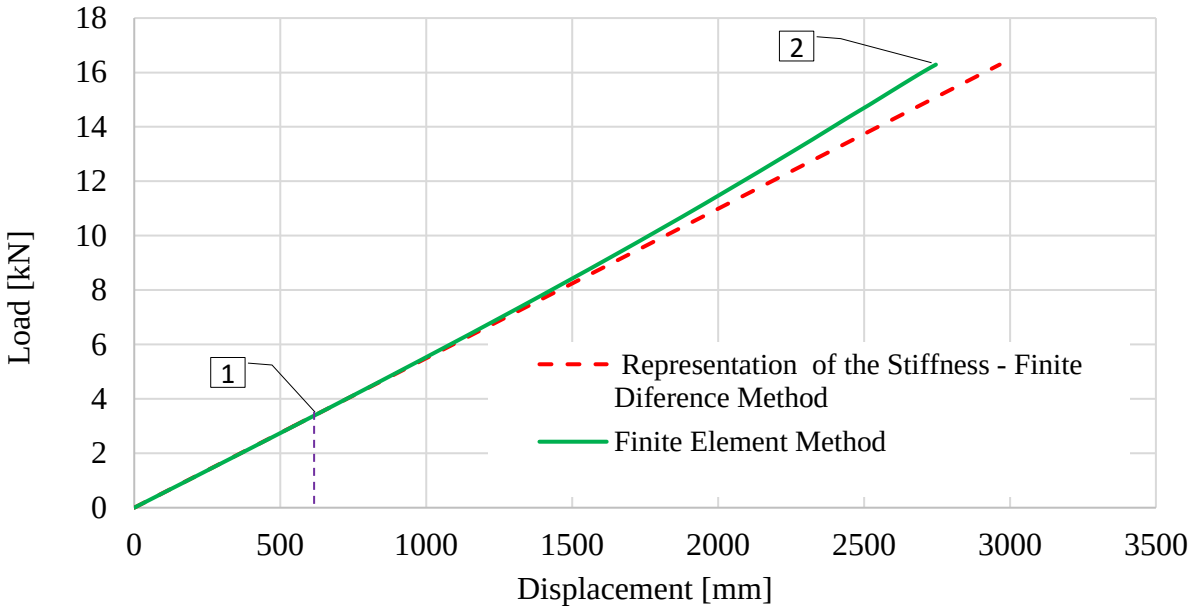

Figure 47: Behavior of pole D

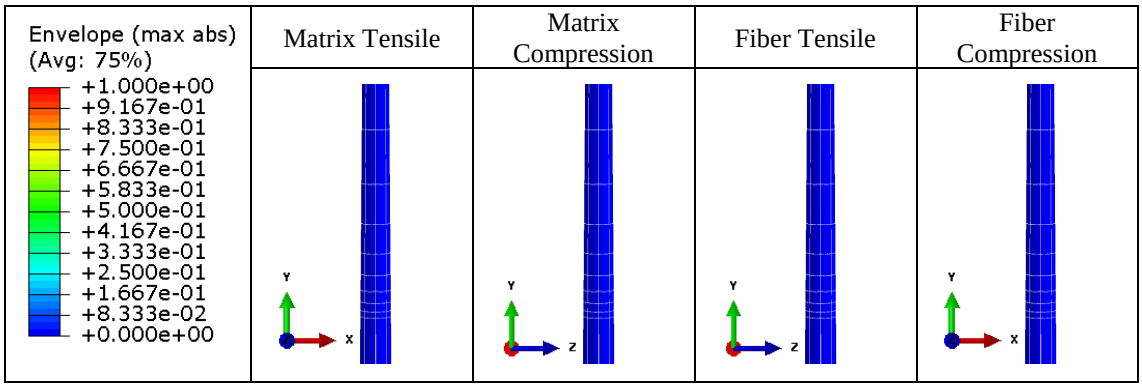

Figure 48: Values of the damage initiation criterion experienced during the analysis for point 1 of Figure 47

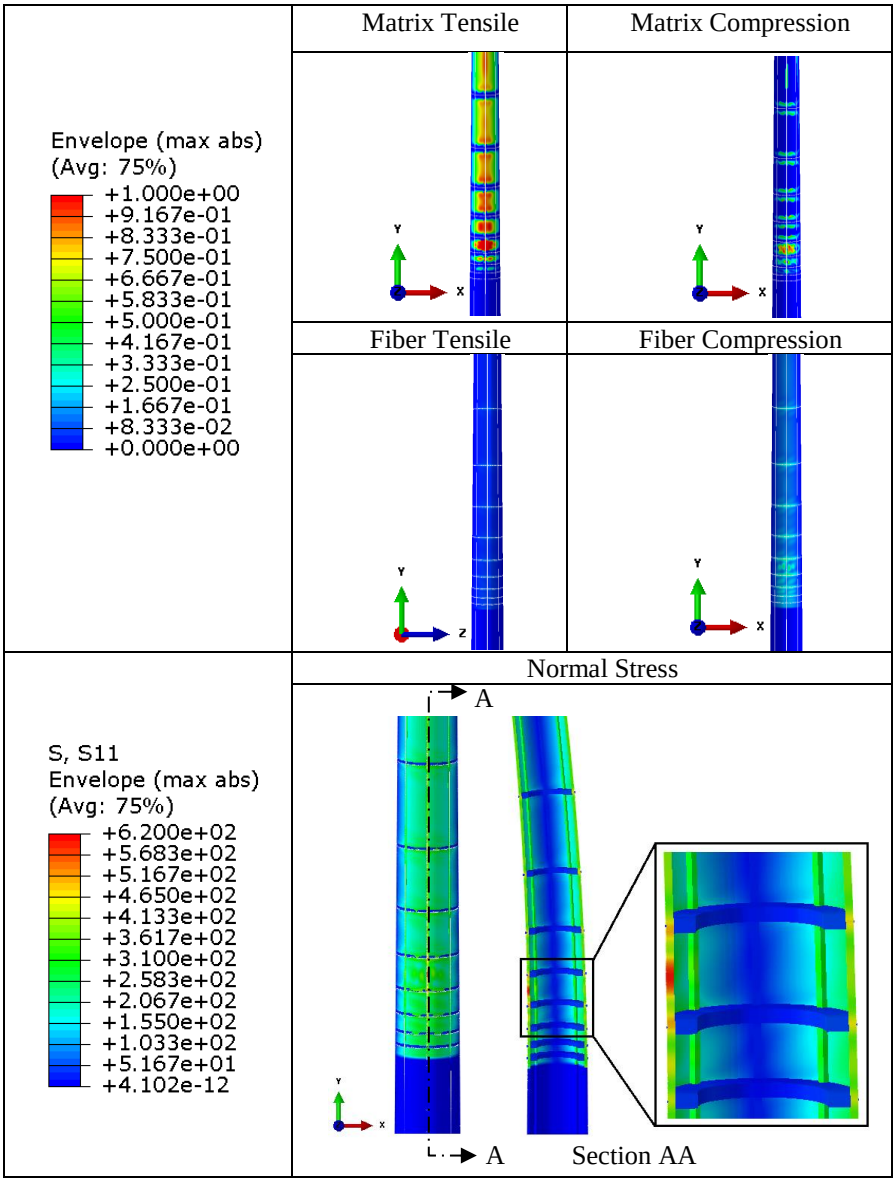

Figure 49: Values of the damage initiation criterion experienced during the analysis for point 2 of Figure 47

6

CONCLUSIONS

In this work, a new pole configuration containing internal rings was studied. The performance of four composite pole configurations was evaluated: monocoque (A), semi-monocoque with stringers (B), semi-monocoque with rings (C) and semi-monocoque with stringers and rings (D). The finite difference method proved to be a good tool to preselected, through the parametric study, the best configurations, which were then studied using the finite element method.

The parametric study conducted showed that, for angles near the longitudinal axis pole axes, the resulting mass for the semi-monocoque poles differs little from the monocoque poles. However, for larger angles, there were significant differences in the resulting masses, comparing the monocoque and semi-monocoque poles with eight stringers. This is due to the fact that, for larger angles, the modulus of elasticity resulting from the pole tends to decrease, since the GFRP has its greatest modulus of elasticity in the fiber direction, and to compensate, the thickness must be increased. The addition of stringers has the advantage of increasing stiffness, since these stringers have the fibers aligned with longitudinal axis.

The FEM analysis with ± 30 ° angles was performed. A good stiffness agreement was obtained when compared to FDM. However, when the displacements increased, the nonlinearity of the problem became more evident, causing the stiffness of the MDF and FEM to begin to differ. The geometric non-linearity was considered in the FEM, using the Riks method. In all cases, the ultimate strength showed to be sensitive to the skin thickness, that is, the skin fails before the stringers. Pole B presented the lowest ultimate load (with skin failure and then in the stringer) due to a condition with the smallest thickness in relation to pole A and pole C. Pole A had a higher failure load than pole B, due the thickness of the shell is greater to resist the loads. Pole D have the same skin thickness as pole B, however, had a higher strength than the poles A and B, showing that the rings had a significant contribution. Thus, pole C obtained the highest

final load, due to besides having the greater thickness than the pole B and D, it has rings, which contributed with the resistance.

Thus, the results shown in this work will provide information on the performance of each configuration that may assist manufacturers to design the composite laminate pole. To complement the information, it is suggested for future work, to construct and to test the models proposed in this work, in addition to considering other geometries.

7

REFERENCES

ALÍPIO, L. G. S. *Projeto e Análise de Postes de Estrutura Semi-monocoque Fabricados com Materiais Compósitos*. Belo Horizonte: UFMG, 2014. 64p.

ALVES, I. G. *Análise do Comportamento Mecânico de Anéis Compósitos Íntegros ou com Defeitos Submetidos a Ensaio de Tração*. Rio de Janeiro: UFRJ, 2006. 138 p.

BECKER, H. *Handbook of Structural Instability Part VI- Strength of Stiffened Curved Plates and Shells*. NACA Technical Note 3786, Washington: New York University, 1958. 82 p.

BIRCHAL, G. A., LAS CASAS, E.B., CIMINI JR., C.A. and TSAI, S.W. *An Alternative Fiber-Reinforced Plastic Pole Design.* Proceedings of the 13th International Conference on Composite Materials, ICCM-13, Beijing, 2001, CD-ROM.

BIRCHAL, G. A. *Postes Autoportantes em Materiais Compostos Poliméricos.* Belo Horizonte: UFMG, 2001. 144 p.

CEMIG - COMPANHIA ENERGÉTICA DE MINAS GERAIS. *Especificação Técnica – Poste em Compósito (poste de poliéster reforçado com fibra de vidro – PRFV).* 2010. 6 p.

CIMINI JR., C.A. and LAS CASAS, E.B. *Disposição Construtiva de uma Estrutura Semimonocoque Confeccionada em Material Composto Polimérico para a Aplicação na Fabricação de Postes*. BR 10 2013 009771 3. 2013. 19p.

CHEN, W. F. and LUI, E. M. L. *Structural Stability. Theory and Implementation*. 1st Edition, PTR Prentice Hall, 1987. 490 p.

Core6. Available in <https://www.core-6.co.uk/structural-profiles/>. Accessed in: July 23, 2018, 14:31.

CUNHA, M. C. *Métodos Numéricos*, 2 ª edição, Editora da Unicamp, Campinas, 2000 p.174.

DANIEL, I.M. and ISHAI, O. *Engineering mechanics of composite materials*, 2nd Edition Oxford University Press, Oxford: 2006. 466p.

DASSAULT SYSTÈMES. *Abaqus Analysis User's Manual*, United States of America: 2014.

DOITRAND, A., FAGIANO, C., CHIARUTTINI, V., LEROY F.H., MAVEL A. and HIRSEKORN M. *Experimental characterization and numerical modeling of damage at the mesoscopic scale of woven polymer matrix composites under quasi-static tensile loading*. Composites Science and Technology, 2015. 11 p.

DOITRAND, A., FAGIANO, C. and IRISARRI, F. X. Comparison between voxel and consistent meso-scale models of woven composites. *Composites Part A: Applied Science and Manufacturing.* Vol. 73, June 2015, p. 143-154.

FAM, A.Z. *Concrete-filled fiber reinforced polymer tubes for axial and flexural structural members*, 2000. Ph.D. thesis, The University of Manitoba, Winnipeg, MB, Canada.

FAM, A., KIM Y.J. and SON, J.K. A numerical investigation into the response of free end tubular composite poles subjected to axial and lateral loads, *Thin-Walled Structures*. Vol. 48, Issue 8, August 2010, p. 651-659.

GAY, D. *Composite Materials, Design and Application* 3.ed. Boca Raton: CCR Press, 2015. p. 17-27.

Globo play, oct 1, 2017. Available in: <https://globoplay.globo.com/v/6186899/> Accessed in 10/05/2018.

HASHIN, Z. Failure criteria for unidirectional fiber composites, *ASME Journal of Applied Mechanics*, Vol. 47 (2), p. 329-334, 1980.

HASHIN, Z. and ROTEM, A. A fatigue Criterion for Fiber-reinforced Materials. *Journal of Composite Materials*. 1973. vol. 7, pp. 448–464.

HIBBELER, R.C., Resistência dos Materiais, 5.ed. Prentice Hall, São Paulo, 2010

IBRAHIM S.M. *Performance evaluation of fiber-reinforced polymer poles for transmission lines*. Ph.D. thesis. Canada: The University of Manitoba, Winnipeg, 2000.

KOPELIOVICH, D. *Pultrusion,* Available in: <http://www.substech.com/dokuwiki/doku.php?id=pultrusion>. Accessed in: Mar 21, 2017.

LAPCZYK I. and Hurtado J. A. Progressive damage modeling in fiber-reinforced materials. *Composites: Part A: applied Science and manufacturing*. Vol. 38, Issue 11, November 2007, Pages 2333-2341.

MATZENMILLER, A.; LUBLINER, J.; TAYLOR, R. L. A constitutive model for anisotropic damage in fiber-composites. *Mechanics of materials*, v. 20, p. 125-152, 1995.

MEGSON, T. H. G. *Aircraft structures for engineering students*. 3rd.ed. Oxford: Butterworth Heinemann, 1999. p. 223.

METICHE, L., MASMOUDI, R. Analysis and design procedures for the flexural behavior of glass fiber-reinforced polymer composite poles. *Journal of Composite Materials.* February, 21, 2012. P. 207-208.

NIU, M.C.Y.; *Airframe Structural Design: Practical Design Information and Data on Aircraft Structures.* California: Conmilit Press Ltd, 1988. p. 376.

Nuplex. Available in <http://www.nuplex.com/composites/processes/filament-winding>. Accessed in: July 23, 2018, 13:53.

PETROFISA DO BRASIL. *Postes em Compósitos, Catálogo do Produto*. 2008. 26 p.

SILVA, S. F. O método das diferenças finitas aplicado à viga de Euler: Comportamento estático e dinâmico. *Revista Traços*. jun. 2008, v.10, n.21. Belém, p. 9-22.

SOARES, A. A. B. *O método das diferenças aplicado à teoria de vigas.* Belém, 2010. 126 p.